bioRxiv preprint doi: https://doi.org/10.1101/2021.06.20.449152; this version posted June 21, 2021. The copyright holder for this preprint (which was not certified by peer review) is the author/funder, who has granted bioRxiv a license to display the preprint in perpetuity. It is made available under aCC-BY-ND 4.0 International license.

Large-scale neural recordings with single-cell resolution in human cortex using high-density Neuropixels probes

AUTHORS

Angelique C. Paulk[1], Yoav Kfir[2], Arjun Khanna[2], Martina Mustroph[2], Eric M. Trautmann[3], Dan J. Soper[1], Sergey D. Stavisky[4], Marleen Welkenhuysen[5], Barundeb Dutta[5], Krishna V. Shenoy[6], Leigh R. Hochberg[1,7], R. Mark Richardson[2], Ziv M. Williams[2]*, and Sydney S. Cash[1]*

AUTHOR INFORMATION

[1]Department of Neurology, Harvard Medical School, Boston, MA, USA; Center for Neurotechnology and Neurorecovery, Department of Neurology, Massachusetts General Hospital, Boston, MA, USA.

[2]Dept. of Neurosurgery, Harvard Medical School and Massachusetts General Hospital, Boston, MA, USA.

[3]Zuckerman Institute, Columbia University, New York, NY; Department of Electrical Engineering, Stanford University, Stanford, CA, USA; Wu Tsai Neurosciences Institute, Bio-X Program, Stanford University, Stanford, CA, USA; Howard Hughes Medical Institute at Stanford University, Stanford, CA, USA.

[4]Department of Neurosurgery, Stanford University, Stanford, CA, USA; Department of Electrical Engineering, Stanford University, Stanford, CA, USA; Wu Tsai Neurosciences Institute, Bio-X Program, Stanford University, Stanford, CA, USA.

[5]IMEC, Leuven, Belgium.

[6]Department of Electrical Engineering, Stanford University, Stanford, CA, USA; Department of Bioengineering, Stanford University, Stanford, CA, USA; Department of Neurobiology, Stanford University, Stanford, CA, USA; Howard Hughes Medical Institute at Stanford University, Stanford, CA, USA; Wu Tsai Neurosciences Institute, Bio-X Program, Stanford University, Stanford, CA, USA.

[7]VA RR&D Center for Neurorestoration and Neurotechnology, Rehabilitation R&D Service, Providence VA Medical Center, Providence, RI, USA; School of Engineering and Carney Institute for Brain Science, Brown University, Providence, RI, USA.

* Co-senior authors

CORRESPONDENCE

Angelique C. Paulk, Sydney S. Cash and Ziv M. Williams

bioRxiv preprint doi: https://doi.org/10.1101/2021.06.20.449152; this version posted June 21, 2021. The copyright holder for this preprint (which was not certified by peer review) is the author/funder, who has granted bioRxiv a license to display the preprint in perpetuity. It is made available under aCC-BY-ND 4.0 International license.

Mail: 55 Fruit St. Boston, MA 02114

Email: apaulk@mgh.harvard.edu, scash@mgh.harvard.edu, zwilliams@mgh.harvard.edu

Number of Figures: 5

Number of Tables: 0

Number of Extended Data Figures and tables: 6

Number of Supplementary Videos: 0

KEYWORDS: Neuropixels, human, single unit, neuron

ABSTRACT

Recent advances in multi-electrode array technology have made it possible to monitor large neuronal ensembles at high resolution. In humans, however, current approaches either restrict recordings to only a few neurons per penetrating electrode or combine the signals of thousands of neurons in local field potential (LFP) recordings. Here, we describe a set of techniques which enable simultaneous recording from over 200 well-isolated cortical single units in human participants during intraoperative neurosurgical procedures using Neuropixels silicon probes. We characterized a diversity of extracellular waveforms with eight separable single unit classes, with differing firing rates, positions along the length of the linear electrode array, spatial spread of the waveform, and modulation by LFP events such as inter-ictal discharges and burst suppression. While some additional challenges remain in creating a turn-key system capable of recording, Neuropixels technology could pave the way to studying human-specific cognitive processes and their dysfunction at unprecedented spatiotemporal resolution.

Major technological advances in the past decade have led to a revolution in the neurosciences. Many research programs now routinely rely on the analysis of single-neuron action potentials from hundreds and even thousands of neurons, which provide a rich understanding of the coordinated activity of large neuronal ensembles that underlie sensory, motor, and cognitive operations [1–4]. While these developments have been most pronounced in animal models, there have been parallel, albeit slower, advances in the ability to record from single neurons in humans. Single-unit recordings in humans have been performed since the mid-1950s [5–8], and played a foundational role in developing an understanding of the role of neural circuits in neurologic disease. For example, such techniques helped to establish an understanding of the

bioRxiv preprint doi: https://doi.org/10.1101/2021.06.20.449152; this version posted June 21, 2021. The copyright holder for this preprint (which was not certified by peer review) is the author/funder, who has granted bioRxiv a license to display the preprint in perpetuity. It is made available under aCC-BY-ND 4.0 International license.

relationship between basal ganglia dysfunction and Parkinson's disease [9]. There are currently at least four high-resolution neuronal recording technologies that can be used in human participants in acute, subacute, and even chronic settings. These include microwire bundles [10,11], an array of microelectrodes arranged in laminar fashion [12,13], microelectrode contacts arranged on a grid for use above the pia or on the shaft of a depth electrode [14–16], and the 'Utah' planar array of penetrating microelectrodes[17–19]. Recent technological developments to move beyond more rigid structures include thin-film based systems with organic polymer electrodes (often referred to as micro-electrocorticography, 'µECoG'), which provide access to surface recordings in the cortex [20–25] and even from the surface of the hippocampus intraoperatively [26].

While each of these approaches is nominally capable of recording action potentials from individual neurons, all are limited to capturing only 10-150 separable units (and often well below 150) per device. In addition, these approaches can rarely isolate action potentials from more than one neuron on a single recording channel (and vice-versa, rarely observe a single neuron from multiple channels), limiting the quality of spike sorting and resulting in limited confidence in isolation efficacy and whether the full range of neurons (including those with small-amplitude waveforms or low firing rates) are being observed. An ideal system would both increase the quantity of neurons an experimenter can record while simultaneously allowing for high quality spike sorting.

Demonstrations of neural recording systems using animal models have advanced at a substantially more rapid pace. A recent landmark for these advances has been the introduction of the silicon Neuropixels probe, a fully-integrated linear silicon microelectrode array with a single 10 mm shank (**Fig. 1a**), which is covered with microelectrode contacts at a 20 µm site-to-site spacing. The Neuropixels 1.0 probes can record 384 user-selectable channels simultaneously from the 24µm x 70µm x 10 mm shank. This system, introduced in 2017, has already enjoyed widespread adoption for recording in rodents [1,2] and non-human primates [3], with continuing improvements to reduce the size and provide additional form factors [4]. Meanwhile, recording single unit activity in humans is increasingly common in research, while also an important tool for clinical care, including the use of real-time neurophysiology to guide deep brain stimulating electrodes for neurological disorders like Parkinson's disease [9,27–34]. Research to develop clinical brain computer interfaces for individuals with severe speech and motor disorders have used Utah arrays to record populations of single neurons and groups of several neurons. These studies have proven instrumental in enabling basic neuroscience and clinical studies at the level of single neurons (though not necessarily well isolated single units) and at the population level, across a variety of contexts ranging from external device control to

bioRxiv preprint doi: https://doi.org/10.1101/2021.06.20.449152; this version posted June 21, 2021. The copyright holder for this preprint (which was not certified by peer review) is the author/funder, who has granted bioRxiv a license to display the preprint in perpetuity. It is made available under aCC-BY-ND 4.0 International license.

handwriting to upper extremity reanimation to improved sensory feedback (via intracortical microstimulation) [35–44]. Adapting the Neuropixels recording system for use in clinical research presents a viable approach for building on these prior demonstrations of the utility of neural recordings with single-cell resolution for developing neurorestorative technologies and expanding our understanding of human cortical function.

We sought to test the efficacy of using Neuropixels probes to record brain activity acutely during clinically indicated neurosurgery, as an important prerequisite step to advanced fundamental neurophysiological investigations and, ultimately, as a clinical tool, such as detailing the single cell mechanisms underlying epilepsy at high spatial resolution[27,30] or changes in cellular interactions induced by tumor cells[45,46]. The versatility of the Neuropixels probe allowed us to record activity both during the placement of deep brain stimulators (DBS) and, separately, during open craniotomies for removal of brain tissue for the treatment of epilepsy or brain tumors.

Here, we demonstrate a set of methods which enable a new, thicker variant of the Neuropixels probes to be used for acute experiments in human patients and use this approach to begin characterizing the diversity of neurons in human cortex, including the dorsolateral prefrontal cortex and temporal lobe. We demonstrate the ability to overcome challenges related to sterilization, electrical isolation, and brain pulsation. We observed a wide diversity of extracellular waveforms (assigned into different putative cell type groupings, validated using three separate clustering techniques). Contrary to prior expectations [47], firing rates only differed slightly between narrow- and wide-waveform amplitude units. We also found single cell activity covaried significantly with epileptiform activity as well as anesthesia-induced burst suppression.

RESULTS

Here, we report successful recordings from the cortex of temporal and frontal lobes in patients undergoing brain tissue resection to treat epilepsy (N=1, under general anesthesia, lateral temporal lobe) or during the implantation of DBS leads to treat movement disorders (N=2, one awake and one under general anesthesia, dorsolateral prefrontal cortex) using Neuropixels probes. We also report unsuccessful recordings – and lessons learned -- from six cases performed while developing these approaches (**Supplemental Table 1; Supplemental Figure 1;** see **Methods**). Unsuccessful recordings were either due to electrode fracture (N=2, with the devices and pieces fully recovered; **Supplemental Table 1**) or excessive noise during the recordings (N=4). Two different types of Neuropixels arrays were used: a thinner Neuropixels 1.0 probe (thickness: 25µm, width: 70µm, length: 10 mm) was utilized in two of the six failed

bioRxiv preprint doi: https://doi.org/10.1101/2021.06.20.449152; this version posted June 21, 2021. The copyright holder for this preprint (which was not certified by peer review) is the author/funder, who has granted bioRxiv a license to display the preprint in perpetuity. It is made available under aCC-BY-ND 4.0 International license.

attempts; neither of these yielded stable recordings. Given the challenges introduced by using such a thin probe in the operating room context, we developed a variation of the Neuropixels 1.0 probe, featuring a 100µm thick shank (Neuropixels 1.0-ST: thickness: 100µm width: 70 µm, length: 10 mm). This version enabled considerably easier insertions and robust use during neurosurgical cases, easing the process of inserting the probe and lowering the risk of mechanical failure. This probe version, combined with an improved grounding and reference electrode configuration enabled us to observe spiking activity from populations of isolatable single neurons in three participants (N=3, **Supplemental Table 1; Supplemental Figure 1;** see **Methods**).

Since the Neuropixels probe is typically used for small animal neurophysiology, five technical developments were needed to translate this device to intraoperative use in people. These included 1) sterilization with ethylene oxide and maintaining sterile conditions, 2) mounting the probe to a neurosurgical robot or a sterile micromanipulator, and 3) stereotactically guided insertion through a burr hole or craniotomy window. These techniques, some of which were informed by our previous experience adapting Neuropixels to NHPs [3], are described in further details in the **Online Methods**. A fourth, and crucial, consideration was the identification and reduction of sources of noise in our recordings in the operating room (OR), which are considerably larger and harder to control than in experimental laboratory settings for animal research. We performed tests both during the neurosurgical cases as well as in the OR without a patient to identify the external sources of noise (e.g. anesthesia IV pumps) as well as internal sources of noise (e.g. we found that in this environment ground and reference should be separate and not tied together has is often required in mouse studies); see **Methods; Supplemental Fig. 1**. Fifth, as it was not possible to suppress the pulsating motion of the brain due to patient safety considerations, a post-hoc registration method was required to ensure stable unit isolations over time.

bioRxiv preprint doi: https://doi.org/10.1101/2021.06.20.449152; this version posted June 21, 2021. The copyright holder for this preprint (which was not certified by peer review) is the author/funder, who has granted bioRxiv a license to display the preprint in perpetuity. It is made available under aCC-BY-ND 4.0 International license.

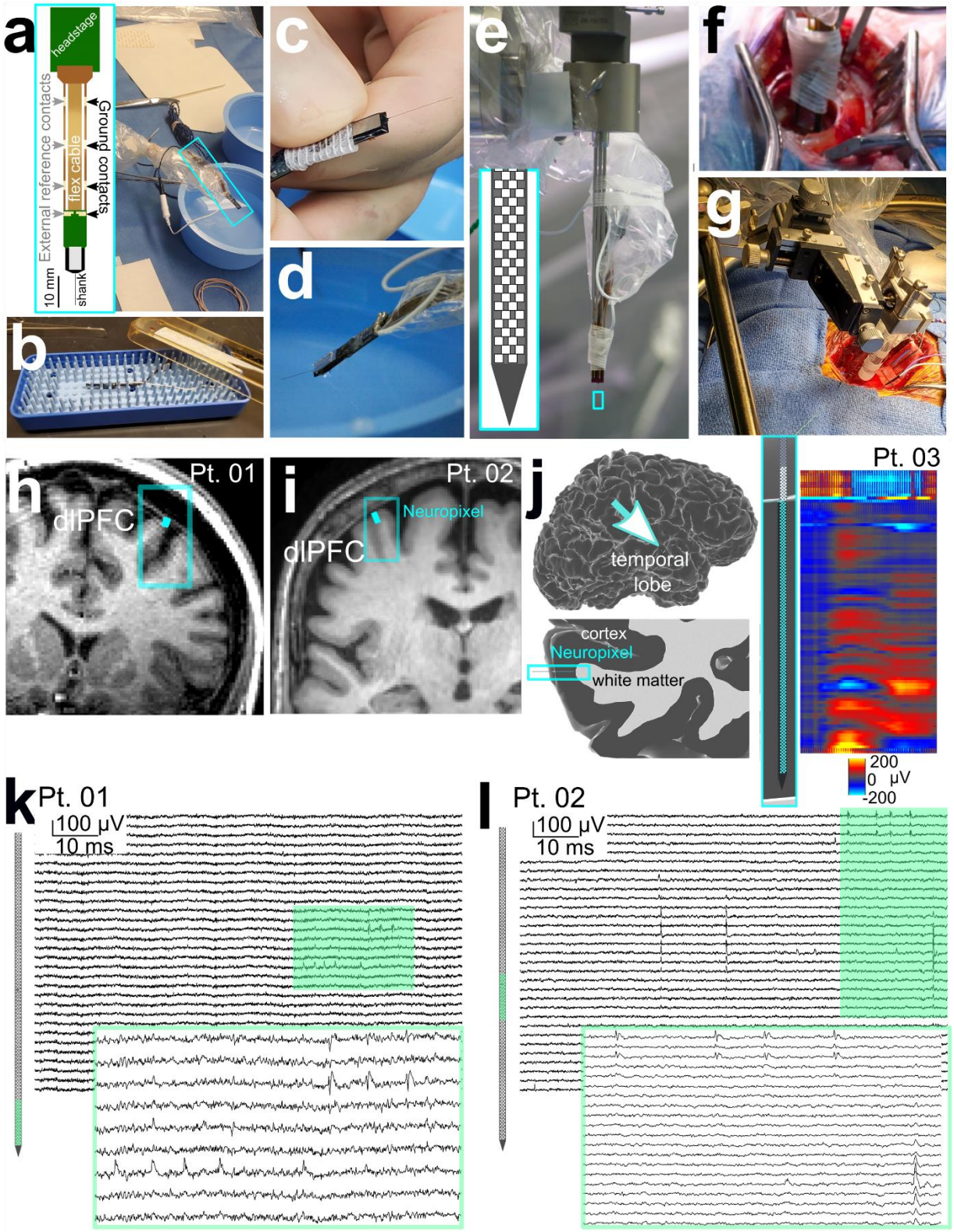

Figure 1: Human neocortical neurons recorded using Neuropixels 1.0-S probes. a-d: Diagram of the Neuropixels 1.0-S probe with a headstage and the ground and reference pads

bioRxiv preprint doi: https://doi.org/10.1101/2021.06.20.449152; this version posted June 21, 2021. The copyright holder for this preprint (which was not certified by peer review) is the author/funder, who has granted bioRxiv a license to display the preprint in perpetuity. It is made available under aCC-BY-ND 4.0 International license.

indicated (outlined in cyan, left) and preparation in a sterile field, with the probe outlined in cyan (**a**), set-up before electrode insertion, including opening the sterile electrode in the packaging, (**b**), handling and connecting to wires and visual inspection (**c**), and testing in saline (**d**). (**e**) Electrode attached to 3 sterile stylets on the ROSA robot for insertion. (**f**)**.** Electrode inserted into the dorsolateral prefrontal cortex (dlPFC) through a burr hole using the ROSA robot. (**g).** Electrode inserted into lateral temporal cortex using a 3-axis micromanipulator attached to a Greenberg retractor. **h-i.** Putative Neuropixels probe location overlaid on the preoperative MRI (top) during two DBS cases. **j**. Putative location and likely depth of the electrode in an open craniotomy case for epilepsy surgery in the lateral temporal cortex (left two columns), with the depth informed by the electrophysiology, where the LFP shows a clear difference between superficial electrodes and deeper contacts, as highlighted here in a color scale indicating voltage. **k-l**. Example recording from participant 1 (Pt. 01) and participant 2 (Pt. 02) in the dlPFC across multiple channels, with action potentials shown extending across multiple channels. The light green filled in box in the background traces are then expanded in the green-outlined voltage traces in the foreground. In **e, h**, **i**, and **j**: cyan rectangles are highlighting the location of the Neuropixels probe.

Single unit waveforms were observed on single Neuropixels probe channels and across multiple channels (**Fig. 1-2**). However, we also observed considerable modulation of the voltage recording related to motion of the brain. This motion primarily results from respiratory and cardiac rhythms, which cause the surface of the brain to move relative to the probe. We observed these movement-related changes in both the LFP and action-potential bands. To confirm that the movement present in the neural recordings was due to tissue movement, we matched the neural recording itself, specifically the LFP band, to the synchronized audio of the EKG and video of the brain.

Critically, the high spatial density of Neuropixels electrodes allows for post-hoc motion correction, and high-quality spike sorting. Estimating the timepoint by timepoint brain position relative to the probe was easiest using the LFP channels. (**Supplemental Fig. 2**). We compared multiple approaches for correcting tissue motion and determined that the optimal approach was to use a manual tracking approach (See **Supplementary Methods**) taking advantage of the high-density sampling and the high temporal resolution of the LFP (**Supplemental Fig. 2**).

Following this movement alignment, we sorted waveforms into clusters using Kilosort 3.0 software [4,48] and extracted an average of 201 ± 151.04 clusters from the recordings. Each cluster presumable represents action potentials generated from a single neuron or very small

bioRxiv preprint doi: https://doi.org/10.1101/2021.06.20.449152; this version posted June 21, 2021. The copyright holder for this preprint (which was not certified by peer review) is the author/funder, who has granted bioRxiv a license to display the preprint in perpetuity. It is made available under aCC-BY-ND 4.0 International license.

number of neurons and has both temporal characteristics (waveform shape) and spatial characteristics (the pattern of waveforms across multiple recording channels). Data from the two participants undergoing DBS implants contained similar numbers of clusters (with the Neuropixels recording from the dorsolateral prefrontal cortex, Pt. 01, not awake: n= 262; Pt. 02, awake: n= 312), while the third participant undergoing an anterior temporal lobectomy yielded considerable fewer (Pt. 03, not awake: n= 29). The clusters were then classified as either multi-unit activity clusters (MUA; Pt. 01: n= 60; Pt. 02: n= 134; Pt. 03: n = 10) or single unit clusters as described in detail below (Pt. 01: n= 202; Pt. 02: n= 178; Pt. 03: n = 19; **Supplemental Fig. 3; Supplemental Table 1**).

We found a diverse set of waveforms within and across participants. Broadly speaking, the waveform clusters could initially be subdivided into those with a dominant positively deflecting or negatively deflecting peaks. We also found numerous neurons with complex, multiphasic waveforms which included double-peaks and triple-peaked waveforms. Some isolated units had more than one type of waveform across the different channels with the ability to record simultaneously from multiple closely spaced electrodes, a single putative unit's voltage changes during action potential generation could be detected as differently shaped waveforms. For example, there were units with positive peaks on some channels and, simultaneously, negative peaks on other channels or double peaks on one channel and single peaks on other channels (**Supplemental Fig. 3**). Finally, clusters' waveforms could be highly localized as well as widely dispersed across electrodes, with waveforms of various durations and amplitudes (**Fig. 1e-f; Fig. 2a; Supplemental Fig. 3**). With the ability to record simultaneously from multiple closely spaced electrodes, a single putative unit's voltage changes during action potential generation was detected as differently shaped waveforms. These phenomena have been previously observed in non-human primates (NHPs; [49] and rodents [1,2,4]), but to the best of our knowledge such a high-resolution view of electrophysiological waveform diversity has not been previously available *in vivo* in people. In the following sections, we describe in more detail the spike-sorting approaches being compared, followed by resulting electrophysiological findings of neurons' spiking relationship with other neurons' spikes and relative to the local field potential (LFP).

Cell type classification based on extracellular waveforms

Considering the diversity of waveforms we observed even in these short recordings, we decided to categorize the cluster waveforms using a three-pronged approach. We used both supervised and unsupervised classification techniques to determine if there are consistent

bioRxiv preprint doi: https://doi.org/10.1101/2021.06.20.449152; this version posted June 21, 2021. The copyright holder for this preprint (which was not certified by peer review) is the author/funder, who has granted bioRxiv a license to display the preprint in perpetuity. It is made available under aCC-BY-ND 4.0 International license.

waveform classes (which could relate to different cell types) across patients and if these classes had different firing or locations along the probe's length. One approach involved separating units based on the polarity and half-peak waveform width of the largest waveform per unit (from the one channel with the largest waveform for that unit) using published unit type definitions (**Fig. 1e-f, 2a-c**, and **Online Methods** [47,50]). In the second approach, we performed principal component analysis (PCA) followed by k-means clustering to isolate clusters with unique waveform shapes (**Fig. 2d-f**). Finally, we used a novel, unsupervised, clustering technique, WaveMAP, which allowed us to automatically identify and separate cell types based on waveform shapes across channels utilizing Universal Manifold Approximation and Projection (UMAP) dimensionality reduction combined with Louvain clustering[51]. For each of these approaches, we identified differences between the putative unit types in their waveform characteristics as well as their spatial location along the probe shank. Each classification approach resulted in different numbers of classes, though the classes did have common features.

Classifying waveforms based on duration and peak direction

We used waveform half-peak width and duration (valley-peak) to separate units into three classes: positive spikes (PS; n=348), versus negative spikes with the later subdivided into negative fast spiking (FS; n=115) or negative regular spiking (RS; n=82) single units based on the peak-trough duration of the largest waveform across channels and the polarity (asterisks in **Fig. 2a-c;** see **Online Methods**) [47,50,52–55]. We also included a fourth category of multi-unit activity (MUA) where the waveforms were mixed across the cluster and the autocorrelation and inter-spike-interval (ISI) distributions were more representative of MUA, which were more uniform in distributions as opposed to single unit distributions (**Fig. 2b**). The peak-trough duration cutoff for FS versus RS units was at 300 µs, which is similar to the cutoff reported previously [47,56,57]. This boundary was also near a boundary in a presumed bimodal distribution of peak-trough durations for events with negative polarity (purple line, **Fig. 2ciii**).

This analysis yielded three different categories of neurons, each of which displayed differences in waveform features and spike rates (**Fig. 2ci, 2e**). First, it is noteworthy that PS units generally had wider waveforms compared to the RS and FS units. The half-peak width was 167.3±55.4 µs for PS and 133.8±70.9 µs for FS + RS, while spike duration was 494.2±175.1 µs for PS and 349.6±222.2 µs for FS and RS; **Fig. 2ciii**. These unit types also showed significant differences in repolarization slope and recovery slope as well as the peak-trough ratio (**Supplemental Fig. 4**). Between these three categories of units (PS, RS, and FS),

bioRxiv preprint doi: https://doi.org/10.1101/2021.06.20.449152; this version posted June 21, 2021. The copyright holder for this preprint (which was not certified by peer review) is the author/funder, who has granted bioRxiv a license to display the preprint in perpetuity. It is made available under aCC-BY-ND 4.0 International license.

the PS unit mean firing rates were significantly higher than those of RS and FS units ($p<0.001$; Wilcoxon rank-sum test; RS: 0.3± 0.27; FS: 0.4±0.59; PS: 1.1±1.35 Hz mean firing rate). FS units trended, though non-significantly, towards slightly higher firing rates than RS units ($p>0.05$; Kruskal-Wallis multiple comparisons test; **Fig. 2e**). The peak-trough ratio was significantly lower for the FS and RS units than PS units (PS: 4.8±2.0 RS: 3.9±1.7; FS: 4.1±1.8; $p<0.001$; Kruskal-Wallis multiple comparison test). For the other waveform measures, the recovery slope was higher in absolute amplitude for the RS units than the FS and PS units, while the repolarization slope was larger for the PS units than RS or PS (**Supplemental Fig. 4)**. These differences in waveform characteristics resemble what has been reported in previously in other species (mice, cats, and macaques)[2,47,55].

Differences in spatial spread of waveform classes

An important feature of the Neuropixels probe is the ability to obtain high spatial sampling, which permits tracking of individual spike propagation and has been used to argue for extracellular identification of back propagating action potentials [1,2,4]. Using published metrics and code [2], we calculated the spatial spread and velocity of the waveforms among the three identified categories of waveforms (**Fig. 2f, ; Supplemental Fig. 4**). We found the spatial spread for the FS and RS units was significantly lower than for the PS units ($p<0.001$; Kruskal-Wallis multiple comparison test). However, in none of the waveform classes was there a significant difference in the velocity of the waves above or below the peak waveform. This pattern suggests that the action potentials being recorded here are generated at the soma (**Supplemental Fig. 4**) [2].

bioRxiv preprint doi: https://doi.org/10.1101/2021.06.20.449152; this version posted June 21, 2021. The copyright holder for this preprint (which was not certified by peer review) is the author/funder, who has granted bioRxiv a license to display the preprint in perpetuity. It is made available under aCC-BY-ND 4.0 International license.

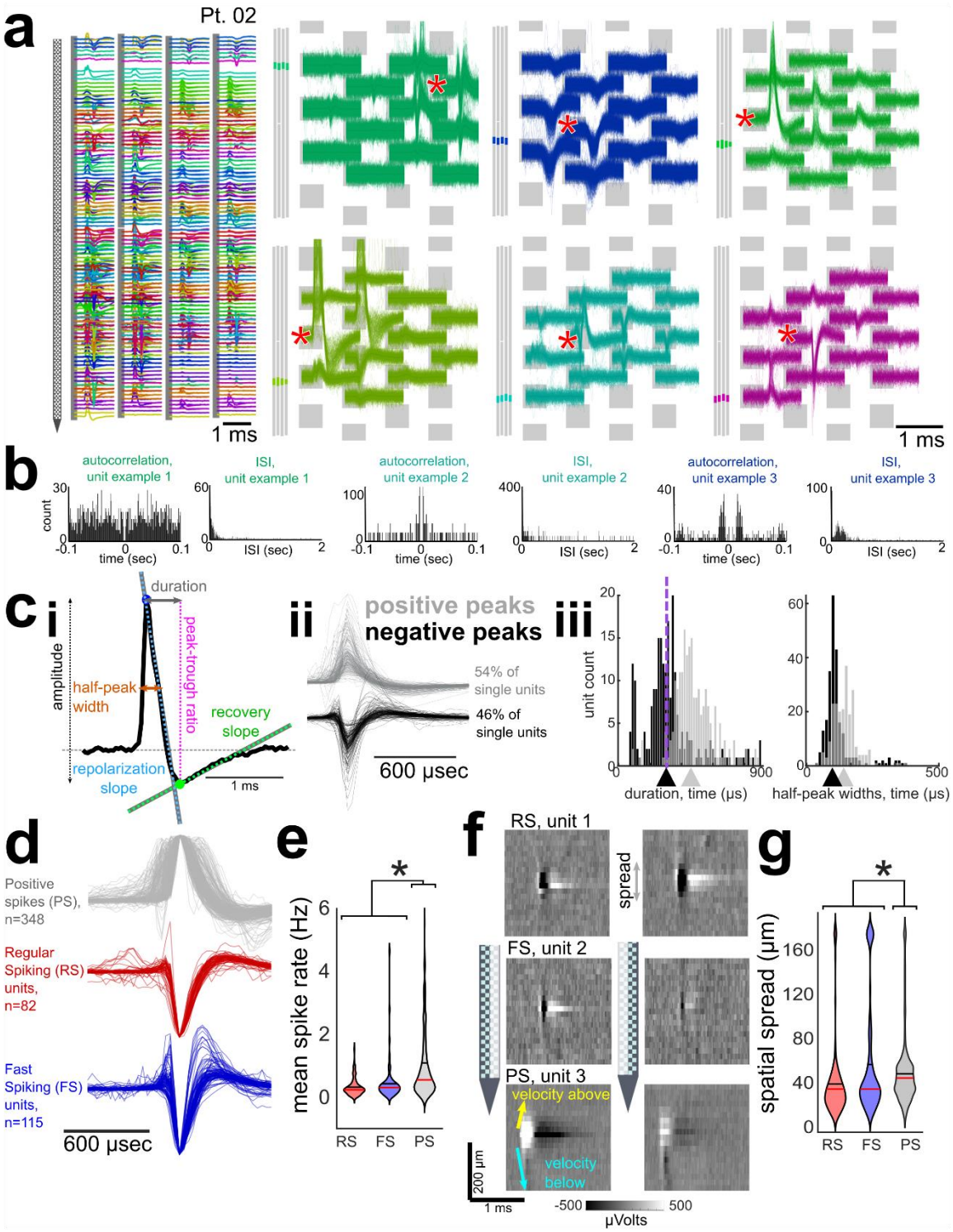

Figure 2: A variety of waveform types and shapes recorded in human neocortex with Neuropixel probes. a. Example unit waveforms (each color is a separate unit, * indicates the largest waveform per unit and this was used for further waveform measurements). On the left, original waveforms are overlaid relative to the recorded channels, with the grey bars to the left

bioRxiv preprint doi: https://doi.org/10.1101/2021.06.20.449152; this version posted June 21, 2021. The copyright holder for this preprint (which was not certified by peer review) is the author/funder, who has granted bioRxiv a license to display the preprint in perpetuity. It is made available under aCC-BY-ND 4.0 International license.

indicating the location of the units along the probe. **b**. Example autocorrelograms and inter-spike-interval (ISI) distributions for three different units. **ci**. Waveform measures on an example, spike waveform including the spike duration, halfwidth, peak-trough ratio, repolarization slope, recovery slope, and amplitude measures. **cii**. Largest waveforms per unit showing positive polarity (grey) and negative polarity (black) waveforms across the data sets. **ciii**. Distribution of positive polarity (grey) and negative polarity (black) half-peak width and spike duration (peak-trough duration) of the largest waveform per unit (Pt. 01-03). **d**. The largest waveform per cluster, color-coded as regular spiking (RS, red), fast spiking (FS, blue), and positive spiking (PS, grey) clusters. **e**. The firing rate distributions for the different groups of putative cell or waveform types across patients. **f**. Spatial spread examples of individual units (averaged across all waveforms attributed to a given unit) across the left and right columns of the Neuropixels probe. Voltage indicated by the greyscale color scheme. Bottom plot: diagram (arrows) demonstrating the spatial mapping calculations, including spatial spread, velocity above (yellow arrow), and velocity below (cyan arrow) the center point (channel with the largest waveform). (Measures shown in **Supplemental Fig. 4**). **g**. Spatial spread of the putative cell or waveform types. In **e** and **g**: * indicate significant differences between putative cell or waveform types, Kruskal-Wallis multiple comparison test, $p<0.001$.

Spatiotemporal waveform classification using PCA and k-means clustering

By focusing on the features of the largest waveform per unit, we are not taking advantage of the high spatial resolution sampling of single cell activity. Therefore, we also used an unbiased clustering approach to classify the units based on each cluster's waveforms across multiple channels, taking into account the spatial spread and other features to classify the units into different groups. (**Fig. 2a, f**). In this alternative clustering approach, we then applied principal components analysis (PCA) to the mean waveforms for each cluster (using a larger feature vector that includes data from multiple electrode sites) per cluster, followed by k-means clustering (**Fig. 3ai; Supplemental Fig. 4**). This analysis identified seven clusters of units using the waveforms from the first six channels of each cluster (with channels reordered-from largest to smallest waveform per unit; **Fig. 3ai-ii**). The resultant classes separated the positive and negative units into varying temporal and spatial distributions as well as triphasic waveforms, with two of the clusters closely resembling the RS and FS designations from the previous analysis, presented above (**Fig. 3ai-ii**). This alternative classification schema also revealed there were increased firing rates for the positive spikes (PS1-3) relative to FS and RS units. In addition, FS firing rates trended higher than RS firing rates (though this did not reach statistical

bioRxiv preprint doi: https://doi.org/10.1101/2021.06.20.449152; this version posted June 21, 2021. The copyright holder for this preprint (which was not certified by peer review) is the author/funder, who has granted bioRxiv a license to display the preprint in perpetuity. It is made available under aCC-BY-ND 4.0 International license.

significance). We found that subsets of positive spikes units (PS1 and PS2) and RS units had increased spatial spread compared to other classes of units (PS3, triphasic units, and FS). We also found similar trends and differences between the PS and other waveforms with increased PS peak-trough ratios and varying repolarization and recovery slopes per waveform classification, though there was no significant difference in velocity (**Fig. 3b; Supplemental Fig. 4**). Finally, mapping the different waveform classes to their location along the probe relative to the surface of the cortex, we found PS units were observed at sites throughout the shank of the probe (and throughout the cortical layers) while the RS and FS type units appeared to be concentrated deeper in the cortex. This spatial distribution of these broad cell categories likely reflects the inhomogeneous distribution of cell types throughout cortical lamina, though a precise mapping of PS, RS, and FS waveform groups to more detailed cell classes is impossible to perform using extracellularly recorded waveforms alone. (**Fig. 3b**).

Clustering waveforms using WaveMap

We also utilized an automated, non-linear method for classifying extracellular waveforms, with the goal of identifying additional classes based on smaller and more nuanced features of the waveforms [51]. Using the WaveMAP algorithm[51], we found that certain waveform types were identifiable across patients. Negative RS and FS-like units were present in all three patient's data, while the positive large waveforms (PS) appeared in two of the three cases (**Fig. 3c; Supplemental Fig. 5**). We therefore pooled the waveforms across patients and clustered waveforms from across the five channels with the largest amplitude waveforms of each unit using WaveMAP which revealed eight total clusters, with four positive spike (PS) clusters and four negative spike clusters. The four negative spike clusters included FS-like, RS-like, triphasic, and broad classes (**Fig. 3c**). As with PCA and k-means clustering, we found little difference in the number of clusters if we included the 6 or 12 channels with the largest amplitude waveforms in the clustering. Interestingly, the WaveMAP classification, revealed differences in spike rates, spatial spread, and depth (along the Neuropixels probe) for different PS units as well as the RS and FS-like units. As we found with the PCA/k-means cluster results, there were subsets of PS units (corresponding to a unique waveform cluster) exhibiting higher spike rates and greater spatial spread. A subset of PS units were located in more superficial cortical lamina relative to the negative spikes and even other PS units (**Fig. 3d; Supplemental Fig. 5**).

bioRxiv preprint doi: https://doi.org/10.1101/2021.06.20.449152; this version posted June 21, 2021. The copyright holder for this preprint (which was not certified by peer review) is the author/funder, who has granted bioRxiv a license to display the preprint in perpetuity. It is made available under aCC-BY-ND 4.0 International license.

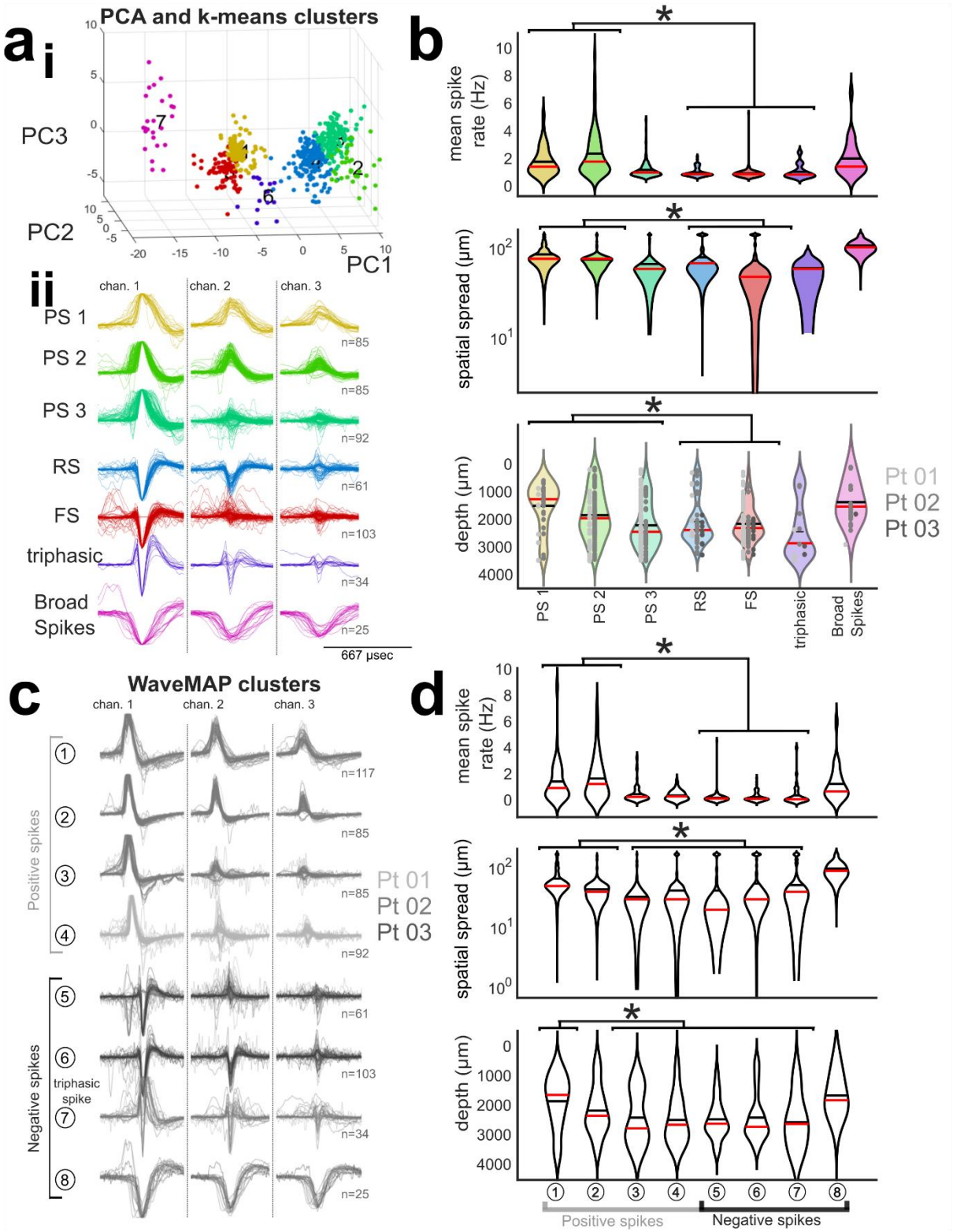

Figure 3: Classifying waveforms based on spatial and temporal features. ai. Scatter plot of seven clusters (using k-means clustering) in the first three principal components. Color coding reflects different clusters. **aii**. Average waveforms per unit, color-coded based on the k-means

bioRxiv preprint doi: https://doi.org/10.1101/2021.06.20.449152; this version posted June 21, 2021. The copyright holder for this preprint (which was not certified by peer review) is the author/funder, who has granted bioRxiv a license to display the preprint in perpetuity. It is made available under aCC-BY-ND 4.0 International license.

clustering with added labels for each waveform type. Columns are the three channels with the largest amplitudes per detected unit. **b**. The mean firing rate, waveform spread, and depth location along the Neuropixels probe for the different k-means-clustered waveforms. The scatter plot for the depth information reflects the data from all three patients, color-coded for each patient: Pt. 01-light grey, Pt. 02-middle grey, Pt. 03-dark grey. **c**. Average waveforms of each unit for the first three channels per unit (each column is a channel), grouped based on the WaveMAP clustering across patients (each detected unit is color coded for recordings from Pt. 01-Pt. 03 (light grey, middle grey, dark grey)). **d**. The firing spike rate, peak-trough ratio, spatial spread, and depth violin plots for the different waveform clusters. Asterisks indicate significant differences between putative cell or waveform types, Kruskal-Wallis multiple comparison test, $p<0.001$, post hoc Tukey-Kramer test for multiple comparisons.

Timing and interactions among single units

From the time of probe insertion, we could observe units within seconds of insertion on in the recording, though there was generally a ~2 minute period of time when both single unit and MUA spike rates would slowly increase in all three participants' recordings before levelling off at a seemingly consistent rate (**Fig. 4a**). We mapped the WaveMAP clustered single units as well as the MUA clusters to the electrode depth and the duration of the recordings (**Fig. 4a**). We found that the different WaveMAP classes could be observed throughout the recording and across the Neuropixels shank (**Fig. 4a**).

To determine if there were interactions between units through time, we performed pairwise covariance analyses between the spike times of different pairs of units and found correlations between individual units in two data sets (Pt. 01 and Pt. 02; **Fig. 4b**) [58,59], suggestive of inter-unit circuit activity. We found that some individual units covaried with each other in time (within a 0.1 sec time window), even between different classes (**Fig. 4b**). Across the WaveMAP clusters, we found an average of 6.9 ± 2.58% of all pairs had a significant covarying relationship (at least one binned peak in the covariance calculations 8 STD above the baseline covariance levels across the recording). Of the pairs with significant covariance relationships, the average absolute lag between the pairs was 0.0022 ± 0.0026 sec. However, a challenge in interpreting these temporal lead/lag relationships is that epileptiform activity or general anesthesia induced burst suppression could have induced correlated cluster activity in 2 of the 3 participants (**Fig. 5**). We anticipate more detailed pairwise relationships between units can be identified in future studies without these confounds.

bioRxiv preprint doi: https://doi.org/10.1101/2021.06.20.449152; this version posted June 21, 2021. The copyright holder for this preprint (which was not certified by peer review) is the author/funder, who has granted bioRxiv a license to display the preprint in perpetuity. It is made available under aCC-BY-ND 4.0 International license.

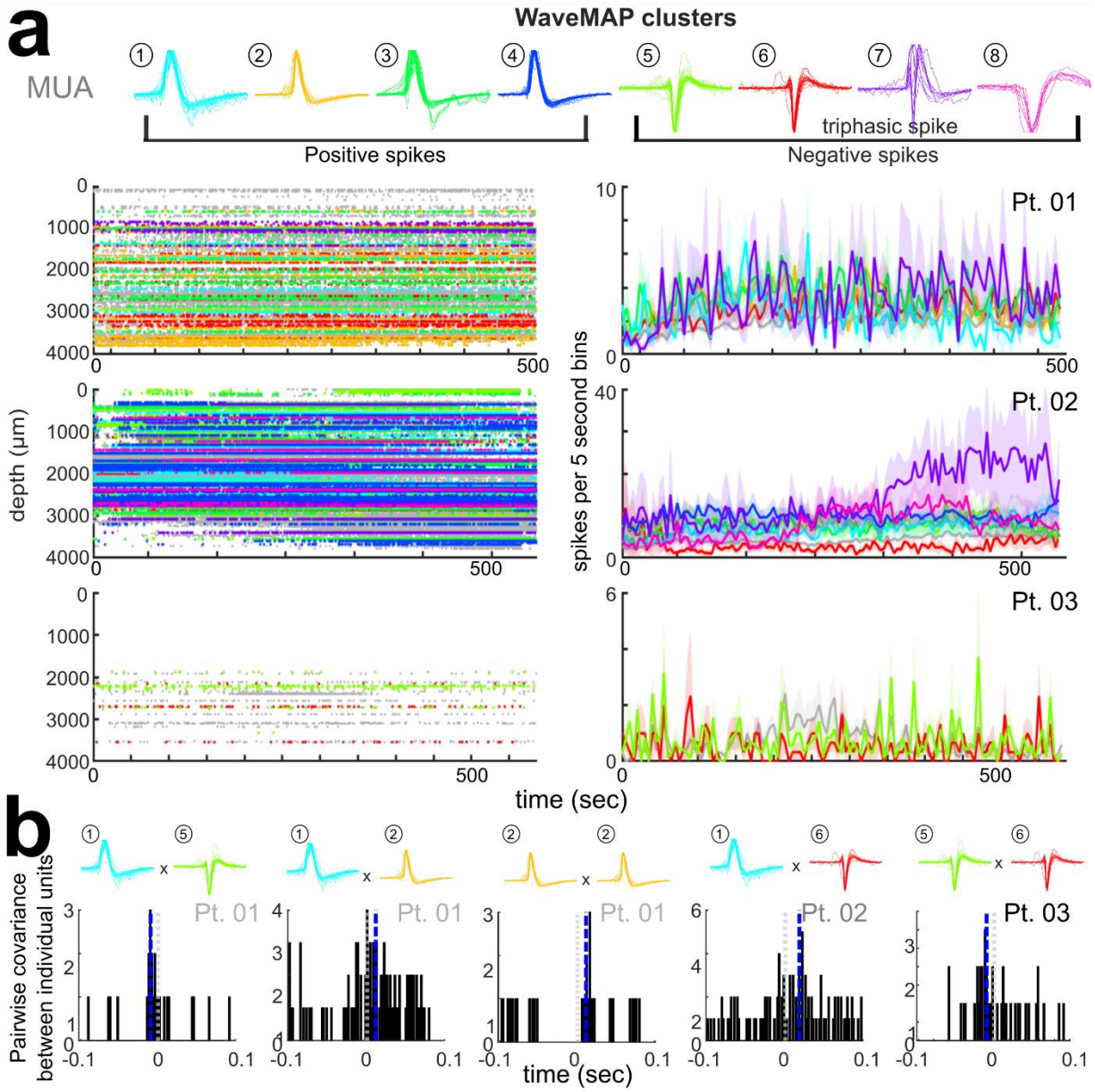

Figure 4. Single units through time and correlation relationships between units. a. Left: the raster plots of spike times throughout the recording for the different classes of single units as clustered by WaveMAP (color coded relative to the waveform from the channel with the largest amplitude per unit) as well as the MUA activity (grey). Right: Spike counts binned in 5 second bins throughout the recordings for the three participants. **b**. Example cross-covariance of the spike times between individual units of different putative classes as clustered by WaveMAP (as titled). The vertical blue line shows the mean per plot.

bioRxiv preprint doi: https://doi.org/10.1101/2021.06.20.449152; this version posted June 21, 2021. The copyright holder for this preprint (which was not certified by peer review) is the author/funder, who has granted bioRxiv a license to display the preprint in perpetuity. It is made available under aCC-BY-ND 4.0 International license.

Neuropixels recordings can reveal spike-field relationships

Numerous questions in clinical and cognitive neuroscience have been addressed by examining the relationships between LFPs and the timing of spikes. To that end, we sought to determine whether the single and multi-units detected using Neuropixels could also be used to extract spike-field relationships (**Fig. 5**). We first movement-corrected the Neuropixels LFP recordings using the same manual approach as for correcting spiking activity which revealed local field voltage reversals along with the Neuropixels depth (**Fig. 5a**).

Even without interpolating and re-aligning the LFP, we could identify interictal epileptiform discharges (IIDs) in the recording from the lateral temporal lobe before tissue resection for epilepsy (**Fig. 5b**). After confirming the presence of the IIDs using both automatic approaches [60] and visual confirmation by a trained epileptologist (SSC), we then aligned the single unit and multiunit activity to the peak of the IIDs (n=57). Single units increased firing around the peak of the IIDs, even in recordings with sparse firing (**Fig. 5c**). To verify this change, we jittered (centered on a normal distribution) the timing of the IID peak relative to the unit times and found that the increase in spike events around the actual IID peaks was significantly above the binned spike times around a jittered IID peak (**Fig. 5d**). Further, we compared the average binned spike counts (across trials per time step) to a baseline -2 to -0.5 sec before the IID and found a significant increase in spikes in the half second after the peak of the IIDs ($p<0.005$; Wilcoxon rank sum test). Some units increased at the IID onset or only fired during the IID peak, while other units decreased firing around or after the IID, though we did not find a correspondence between unit class and spike rate modulation around the IIDs. This varying pattern amongst units has also been reported in Utah array recordings [13].

In two cases, the participants were under general anesthesia, which produced a typical burst suppression pattern in the average LFP (**Fig. 5e-f**; **Supplemental Table 1**; [61]). Single unit firing increased during the bursts and decreased during the suppression periods in the LFP. The firing rate from -1.5 to -0.5 seconds before the onset of a detected burst relative to the -0.5 to +1 seconds after the onset of the detected burst was significantly increased. The unit firing during the bursts was significantly higher compared to the burst-triggered unit firing calculated in a time-shuffled data set, where the burst time onset was shuffled in time relative to the spike data (1000 shuffled tests, **Fig. 5g**). This population change could also be observed at the level of individual units, where the firing rates of single units would increase before, during, and after (depending on the unit) the burst onset time in both patients (**Fig. 5h**). Interestingly, between 25-55% of the individual units within different WaveMAP unit classifications groupings demonstrated significant spike rate modulation relative to the burst onset.

bioRxiv preprint doi: https://doi.org/10.1101/2021.06.20.449152; this version posted June 21, 2021. The copyright holder for this preprint (which was not certified by peer review) is the author/funder, who has granted bioRxiv a license to display the preprint in perpetuity. It is made available under aCC-BY-ND 4.0 International license.

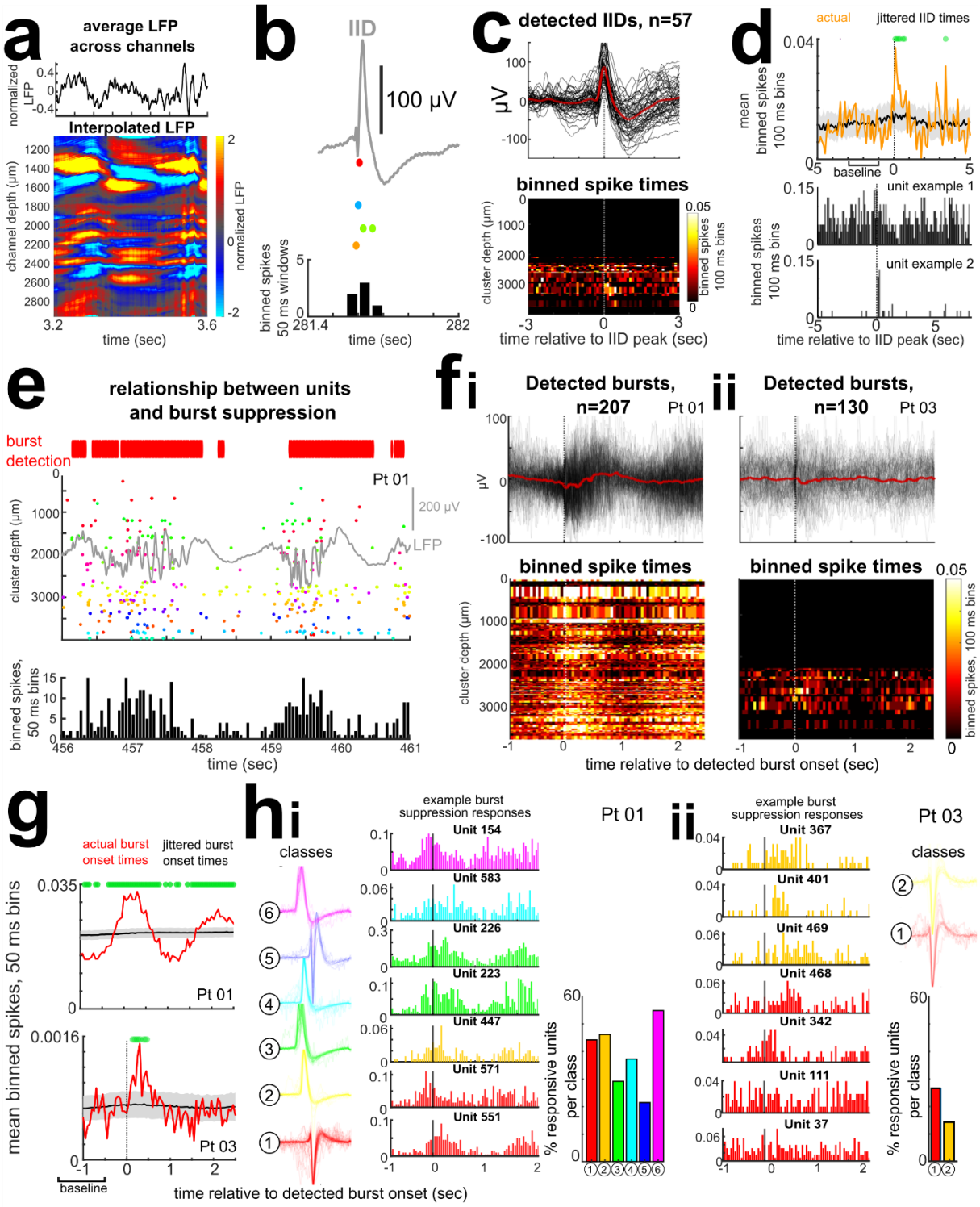

Figure 5. Relationship of units to the local field potential (LFP) events and epileptiform discharges. a. Example LFP averaged across the electrode (top) and along the depth of the Neuropixels probe after interpolating the LFP using manual registration. **b.** Inter-ictal

bioRxiv preprint doi: https://doi.org/10.1101/2021.06.20.449152; this version posted June 21, 2021. The copyright holder for this preprint (which was not certified by peer review) is the author/funder, who has granted bioRxiv a license to display the preprint in perpetuity. It is made available under aCC-BY-ND 4.0 International license.

epileptiform discharge example (IIDs, grey line) along with single unit activity (colored dots represent spike times for different units) through time in Pt. 03, and binned spike times (below). **c.** Top: Individual (black traces, n=57) and average IIDs (red line). Bottom: Binned spike rates of individual units along the Neuropixels depth (y-axis), with the brighter pixels indicating increased activity aligned to the peak of the IIDs. **d**. Individual unit example spike timing relative to the peak of the IIDs. **e.** LFP burst suppression in a participant under general anesthesia, as shown by the grey line (LFP) along with the detected single unit activity (raster plot in the middle figure; each color represents a different unit) and binned into 50 ms windows (bottom). Red bars on top of the figure: automated burst detection algorithm [62]. **fi-ii.** Detected burst onsets relative to binned single unit activity along the Neuropixels probe in two different patients (Pt. 01, **i**, and Pt. 03, **ii**). **g.** Binned spike rates relative to the burst onset (red) compared to time points where the burst onset was jittered randomly around a normal distribution of time ranges (black line). Green dots: spike rates (mean across units) which are significantly different compared to the -1.5 to -0.5 sec before burst onset. **hi**. Left: Units separated into 6 classes for one patient (Pt. 01), color-coded per cluster. Middle: example unit activity relative to the 1 second before and 2 seconds after the burst. Some units increase spiking before, during, or after the burst. Right: Bar graph indicating the percentage of units per class with significant changes in firing rate relative to the burst onset. **hii**. Units separated into 2 clusters for one patient (upper right, Pt. 03), color-coded per cluster, and example unit activity with changes in spike rates relative to the 1 second before the burst onset, with some units increasing spiking before, during, or after the burst. Below right: bar graph indicating the percentage of units per class with significant changes in spike rate relative to the burst onset.

DISCUSSION

Here, we demonstrate that, the broadly available Neuropixels probes can be adapted for use in acute recordings of neuronal activity in the human cortex in an operating room environment. We found that, within minutes after inserting the Neuropixels probe into cortical tissue, we can observe 10s to more than 200 clear and stable units. We could separate units based on waveform shapes (using duration and polarity), and we could also cluster the waveforms using unbiased clustering via PCA with k-means clustering and, separately, using a novel nonlinear clustering approach, WaveMAP [51]. Similar waveform clusters were found across participants using each of the three separate classification approaches, indicating there were consistencies between individuals. This waveform diversity presumably relates to both

bioRxiv preprint doi: https://doi.org/10.1101/2021.06.20.449152; this version posted June 21, 2021. The copyright holder for this preprint (which was not certified by peer review) is the author/funder, who has granted bioRxiv a license to display the preprint in perpetuity. It is made available under aCC-BY-ND 4.0 International license.

differences in cell types and differences in where electrical activity is recorded (e.g., near soma versus axons) [51].

Historically, single-channel extracellular recordings have led to categorizing neurons into inhibitory vs. excitatory / pyramidal neuron classes. Since Cajal's work, we have known that there are subclasses of these types based on location in the cortex, channel expression, morphology and more. It is possible that with this very high-density recording approach enabled by Neuropixels we can make strides towards associating electrophysiologically identified cell types with some of these detailed neuronal subtypes[63–65]. Future work in both animal models and humans will be necessary to correlate functional differences in waveform morphology with essential cellular characteristics. In addition, even with this small sampling, we could find evidence of pairwise covariance between units, which is encouraging in that further data collection and analyses may provide detailed microcircuit maps of human cortex made entirely possible by the high spatial sampling of the Neuropixels probe.

We also observed significant relationships between the LFP bursts and unit spiking activity, with some units' firing increasing even before the burst and others firing during and after. This possibly indicates a circuit-scale phenomenon that warrants further investigation as it may relate to the mechanism of burst-suppression in anesthesia [66]. Also, we found some units would fire at and after an IID, indicating that the Neuropixels probe could capture clinically relevant activity in the LFP while sampling high resolution information about single cells, even acutely in the operating room and even in Pt.03's recording where we "only" isolated a relatively fewer 29 units from this single probe.

Contrary to expectations based on previous reports from the primate literature, we did not observe a reliable bi-modal distribution of spike waveform duration. Historically, a bi-modal distribution has been used to identify putative pyramidal and inhibitory neurons (e.g. [56]), but we did not find strong differences in firing rate for the RS versus FS units, as has been previously reported in the literature [47,50,56,57,67]. While such a separation has been reported with Utah arrays in humans [50,67], we saw no evidence of this distribution in the recordings reported here. One possible explanation is that the higher density of Neuropixels allows more sensitive neuron detection, which leads to recording a wider range of neurons with less bias towards large waveform action potentials. A second (not mutually exclusive) possibility is that this difference is due to the Neuropixels probe sampling across cortical layers, versus the more within-layer sampling of Utah arrays.

A third possibility, and an important component of Neuropixels recordings in the OR, and a consideration when examining activity across cortical layers, is that the range of possible

bioRxiv preprint doi: https://doi.org/10.1101/2021.06.20.449152; this version posted June 21, 2021. The copyright holder for this preprint (which was not certified by peer review) is the author/funder, who has granted bioRxiv a license to display the preprint in perpetuity. It is made available under aCC-BY-ND 4.0 International license.

probe angles and placement relative to gyri and sulci are both significantly increased by the flexibility of the small Neuropixels form factor in penetrating neural tissue from different angles (although approach trajectories are limited by the clinical considerations and access boundaries). In most cases, we could only approach the tissue with a limited set of angles (e.g. limited by the Burr hole) or penetrate a curved surface (with gyri more complex in humans compared to NHPs and mice), such that we may not be as perpendicular to the cortical layers as in NHP or mouse studies [1,3]. One advantage of the Neuropixel probes' single-shank form factor is that it allows for considerable flexibility in the angle and direction of the insertion compared to a planar array like the Utah array[17]. This additional flexibility of insertion configurations, however, introduces additional challenges for recording the spatial location and angular orientation of the probe. This requires additional measurement and documentation of these degrees of freedom, including: 1) mapping to whatever stereotactic placement system is used in 3D, 2) 3D reconstruction of the brain and Neuropixels probe relative to trajectories and photographs (from multiple angles, made possible with the use of Blender), and 3) the use of LFP (**Fig. 1**) and/or the use of different Neuropixels recording maps to define recording depth and boundaries. This approach could be additional refined in future experiments by using the BrainLab software package (Munich, Germany) or other intraoperative visualization tools [68] to improve the mapping precision and fidelity.

For intraoperative research where time constraints can be substantial, there is a high priority on being able to achieve high fidelity, stable recordings quickly. Previous experiences suggest that this may be hampered by cortical 'stunning' which results in few units being recorded for minutes or even longer after electrode insertion [40]. With the Neuropixels probe, however we were able to record large numbers of units within minutes of insertion. In two cases, we recorded more than 200 single units in a period of 5-10 minutes, while, in the third case, we recorded 29 units in a similar time span (10 minutes). The possible difference in the third participant was that the electrode was placed in the lateral temporal lobe to be resected for epilepsy and the patient was deeply anesthetized (as indicated by the high level of suppression in the detected burst-suppression waves).

In addition to being able to record from large numbers of units, the Neuropixels arrangement allows for resolution of units and LFP at different cortical depths. It was clear that distinct types of units are distributed differently across the recording probe, with a possibility that we could also record backpropagating action potentials. Indeed, the dense sampling allows identifying many pairs of interacting neurons (i.e., those exhibiting a consistent temporal lead/lag). Previous reports of groups using Neuropixels to observe backpropagating action

bioRxiv preprint doi: https://doi.org/10.1101/2021.06.20.449152; this version posted June 21, 2021. The copyright holder for this preprint (which was not certified by peer review) is the author/funder, who has granted bioRxiv a license to display the preprint in perpetuity. It is made available under aCC-BY-ND 4.0 International license.

potentials, combined with the present results confirming the ability to super-sample action potentials across multiple electrodes, indicates that similar *in vivo* investigations of human action potential variants are possible [2]. In addition, further analyses of the LFP alone could be mapped to sinks and sources using current source density techniques [69,70,71].

While our Neuropixels recordings of single and multi-unit activity in humans are promising, we found that several important issues will need to be addressed before this approach can be implemented as a turn-key system that will make it easier for more groups to adopt this technique. As expected, we encountered substantial challenges with the electrically noisy environment of the operating room. This required flexibility in the arrangement of the ground and reference electrodes for the recordings. Another major challenge is impact of brain movement on the recordings. Here, we were able to perform a post-hoc manual analysis to mitigate the artifact introduced by brain pulsation and have shared detailed instructions with code (see **Online Methods**). While this was sufficient to allow for accurate spike sorting for the units reported in this analysis, it is likely that many theoretically isolatable units with smaller signals were rejected or ignored due to the challenge of isolating small waveforms across drift events. We found that we could not rely on alignment approaches that only used spike rates[4], since the movement artifact was considerably faster than the 1-2 seconds needed for published stabilization approaches[4]. This is because the problem is not one of drift (i.e. slow displacement of the electrode) but of pulsation artifact due to the ejection of blood into the great vessels with each heartbeat. Our manual approach provided a reasonable fix for this problem but can likely be improved. To this end, we have provided open-source de-identified data which we hope will allow groups to develop/update automated alignment algorithms to work well with these new type of human electrophysiology data. Future work to automatically adjust for movement artifacts would ideally use the voltage fluctuations in the LFP, or a combination of LFP and spike rates, to align the channels and adjust for the movement.

Other methods currently under development to address this challenge aim to directly minimize the tissue motion during the recordings. Most of these approaches focus on mechanically stabilizing the cortex around the probe. Another approach would be to allow the recording electrodes to move with the brain, e.g. as developed by Neuralink [72] or with a flexible link isolating the probe from any positioning equipment or cables. We believe that further development of motion stabilization techniques -- in a manner which optimizes maximizing patient safety – is a top priority and will result in substantially more recorded neurons, each sampled and isolated with more consistency. Lastly, alternative electrode configurations, such

bioRxiv preprint doi: https://doi.org/10.1101/2021.06.20.449152; this version posted June 21, 2021. The copyright holder for this preprint (which was not certified by peer review) is the author/funder, who has granted bioRxiv a license to display the preprint in perpetuity. It is made available under aCC-BY-ND 4.0 International license.

as the linear column configuration used in the Neuropixels 2.0 probe [4] specifically to facilitate automated post-hoc motion correction, will likely help to address this challenge.

A further challenge to applying this technology in intraoperative studies is the necessary time constraints on the recordings. For patient safety, it is not appropriate to extend their time in the operating room significantly. Consequently, we were unable to record beyond ~15 minutes. In the future, this may be extended slightly, depending on the exact surgical context. For example, extensive language mapping in an awake tumor resection case may go on significantly longer. However, the short recordings could be a factor in the waveform shapes we observed (e.g., cell types that fire infrequently or only in certain contexts would be less likely to be observed). Studies in other species could indicate optimal recording stability is achieved at considerably longer recordings (45 minutes)[3]. While we cannot change this feature of our studies, we note it is a potential factor that affects our recordings. This open question presents an opportunity for comparable studies in NHPs or large animals to examine single units in those first moments of insertions, and then afterwards, in order to help us better contextualize human Neuropixels recordings.

Nevertheless, the fact that we obtained single unit-resolution recordings almost immediately upon insertion of the Neuropixels is highly encouraging, since it ensures that useful information can still be obtained in a short period of time. Indeed, the power of these acute tests in the OR using Neuropixels probes will be realized with experiments in which awake subjects engage with a task during the recording period. All such uses cases, however, necessarily build on a demonstration of the feasibility of acute recordings in clinical settings given the unique challenges in this environment. We also note the potential for Neuropixels (or future variants) to accelerate clinical electrophysiology thanks to their dramatically increased channel counts relative to single- or low channel count probes. For example, simultaneously recording along a probe during deep brain stimulation targeting instead of “searching” with single electrodes would reduce procedure time and potentially improve patient outcomes. Additional research avenues can be opened by technological advances necessary to create a chronic form of the system.

In summary, these data imply that substantial circuit details can be untangled using this method in humans. The Neuropixels approach suggests a pathway forward for increasingly sophisticated and detailed explorations of the cellular-scale code underlying higher order cognitive function in multiple areas of the human brain, as well generating a deeper understanding of the dynamics of clinically relevant neural activity. It is also a step towards developing high channel count chronic neural interfaces for human use which may accelerate and expand the therapeutic possibilities of brain-computer interfaces [73].

bioRxiv preprint doi: https://doi.org/10.1101/2021.06.20.449152; this version posted June 21, 2021. The copyright holder for this preprint (which was not certified by peer review) is the author/funder, who has granted bioRxiv a license to display the preprint in perpetuity. It is made available under aCC-BY-ND 4.0 International license.

Extended Data / Supplementary Information

Online Methods

Supplemental Table 1. Distribution and numbers of cases and results as well as reasons for data exclusion and information per participant and recording

Supplemental Figure 1. Recording challenges and lessons learned.

Supplemental Figure 2: Realigning the data relative to heartbeat-induced movement artifact.

Supplemental Figure 3. Example complex waveforms for six different units (each color-coded set of waveforms) across the data set

Supplemental Figure 4. Waveform measures and PCA with k-means clustering

Supplemental Figure 5. Waveform Features of Units Clustered with WaveMAP

Acknowledgements

We would like to thank Yangling Chou, Aaron Tripp, Fausto Minidio, Alex Zhang, and Alexandra O'Donnell for help in data collection. We would like to especially thank the patients for their willingness to participate in this research. This research was supported by the ECOR and K24-NS088568 (to SSC) and the Tiny Blue Dot Foundation (to SSC and ACP). The views and conclusions contained in this document are those of the authors and do not represent the official policies, either expressed or implied, of the funding sources.

Author disclosures

K.V.S. is a consultant to Neuralink Corp. and CTRL-Labs Inc. (now a part of the Facebook Reality Labs division of Facebook) and on the Scientific Advisory Boards of Mind-X Inc., Inscopix Inc. and Heal Inc. The MGH Translational Research Center has a clinical research support agreement with Neuralink, Paradromics, and Synchron, for which S.S.C. and L.R.H. provide consultative input. B.D. and M.W. are employees of IMEC, a nonprofit research institute that manufactures, sells, and distributes the Neuropixels probes, at cost, to the research community.

Author Contributions

The experiment was conceived by SSC, YK, ACP, ZW, KVS, LRH, EMT, and SDS. ZW and RMR performed the surgeries and placed the arrays while ACP, MM, AK, and YK collected the data and did first pass analysis. BD, MW, and EMT conceived of and advanced the production

bioRxiv preprint doi: https://doi.org/10.1101/2021.06.20.449152; this version posted June 21, 2021. The copyright holder for this preprint (which was not certified by peer review) is the author/funder, who has granted bioRxiv a license to display the preprint in perpetuity. It is made available under aCC-BY-ND 4.0 International license.

of the thicker custom Neuropixels probes used in the study. All the authors edited the manuscript.

REFERENCES

1. Jun, J. J. *et al.* Fully integrated silicon probes for high-density recording of neural activity. *Nature* **551**, 232–236 (2017).
2. Jia, X. *et al.* High-density extracellular probes reveal dendritic backpropagation and facilitate neuron classification. *J. Neurophysiol.* **121**, 1831–1847 (2019).
3. Trautmann, E. M. *et al.* Accurate Estimation of Neural Population Dynamics without Spike Sorting. *Neuron* **103**, 292-308.e4 (2019).
4. Steinmetz, N. A. *et al.* Neuropixels 2.0: A miniaturized high-density probe for stable, long-term brain recordings. *Science* **372**, eabf4588 (2021).
5. Ward, A. A. & Thomas, L. B. The electrical activity of single units in the cerebral cortex of man. *Electroencephalogr. Clin. Neurophysiol.* **7**, 135–136 (1955).
6. Marg, E. & Adams, J. E. Indwelling multiple micro-electrodes in the brain. *Electroencephalogr. Clin. Neurophysiol.* **23**, 277–280 (1967).
7. Rayport, M. & Waller, H. J. Technique and results of micro-electrode recording in human epileptogenic foci. *Electroencephalogr. Clin. Neurophysiol.* Suppl 25:143+ (1967).
8. Rayport, M., Buser, P., Bancaud, J. & Talairach, J. Contribution of micro-physiological stereotaxic recording to the study of the inter-ictal and ictal cortical discharge in human epilepsy. *Electroencephalogr. Clin. Neurophysiol.* **26**, 638 (1969).
9. Amirnovin, R., Williams, Z. M., Cosgrove, G. R. & Eskandar, E. N. Experience with microelectrode guided subthalamic nucleus deep brain stimulation. *Neurosurgery* **58**, ONS96-102 (2006).
10. Verzeano, M., Crandall, P. H. & Dymond, A. Neuronal activity of the amygdala in patients with psychomotor epilepsy. *Neuropsychologia* **9**, 331–344 (1971).

bioRxiv preprint doi: https://doi.org/10.1101/2021.06.20.449152; this version posted June 21, 2021. The copyright holder for this preprint (which was not certified by peer review) is the author/funder, who has granted bioRxiv a license to display the preprint in perpetuity. It is made available under aCC-BY-ND 4.0 International license.

11. Fried, I. *et al.* Cerebral microdialysis combined with single-neuron and electroencephalographic recording in neurosurgical patients. *J. Neurosurg.* **91**, 697–705 (1999).
12. Ulbert, I., Halgren, E., Heit, G. & Karmos, G. Multiple microelectrode-recording system for human intracortical applications. *J. Neurosci. Methods* **106**, 69–79 (2001).
13. Keller, C. J. *et al.* Heterogeneous neuronal firing patterns during interictal epileptiform discharges in the human cortex. *Brain* **133**, 1668–1681 (2010).
14. Worrell, G. A. *et al.* High-frequency oscillations in human temporal lobe: Simultaneous microwire and clinical macroelectrode recordings. *Brain* **131**, 928–937 (2008).
15. Despouy, E. *et al.* Neuronal spiking activity highlights a gradient of epileptogenicity in human tuberous sclerosis lesions. *Clin. Neurophysiol.* **130**, 537–547 (2019).
16. Wicks, R. T. *et al.* Hippocampal CA1 and CA3 neural recording in the human brain: Validation of depth electrode placement through high-resolution imaging and electrophysiology. *Neurosurg. Focus* **49**, 1–10 (2020).
17. Nordhausen, C. T., Rousche, P. J. & Normann, R. A. Optimizing recording capabilities of the Utah Intracortical Electrode Array. *Brain Res.* **637**, 27–36 (1994).
18. Nordhausen, C. T., Maynard, E. M. & Normann, R. A. Single unit recording capabilities of a 100 microelectrode array. *Brain Res.* **726**, 129–140 (1996).
19. Maynard, E. M., Nordhausen, C. T. & Normann, R. A. The Utah Intracortical Electrode Array: A recording structure for potential brain-computer interfaces. *Electroencephalogr. Clin. Neurophysiol.* **102**, 228–239 (1997).
20. Khodagholy, D. *et al.* NeuroGrid: recording action potentials from the surface of the brain. *Nat. Neurosci.* **18**, 310–315 (2015).
21. Khodagholy, D. *et al.* Organic electronics for high-resolution electrocorticography of the human brain. *Sci. Adv.* **2**, e1601027 (2016).

bioRxiv preprint doi: https://doi.org/10.1101/2021.06.20.449152; this version posted June 21, 2021. The copyright holder for this preprint (which was not certified by peer review) is the author/funder, who has granted bioRxiv a license to display the preprint in perpetuity. It is made available under aCC-BY-ND 4.0 International license.

22. Ganji, M. *et al.* Development and Translation of PEDOT:PSS Microelectrodes for Intraoperative Monitoring. *Adv. Funct. Mater.* **28**, 1700232 (2017).

23. Hermiz, J. *et al.* Sub-millimeter ECoG pitch in human enables higher fidelity cognitive neural state estimation. *NeuroImage* **176**, 454–464 (2018).

24. Rogers, N. *et al.* Correlation structure in micro-ECoG recordings is described by spatially coherent components. *PLoS Comput. Biol.* **15**, 1–21 (2019).

25. Paulk, A. C. *et al.* Microscale Physiological Events on the Human Cortical Surface. *Cereb. Cortex* (2021) doi:10.1093/cercor/bhab040.

26. Kleen, J. K. *et al.* Bidirectional propagation of low frequency oscillations over the human hippocampal surface. *Nat. Commun.* **12**, 2764 (2021).

27. Truccolo, W. *et al.* Single-neuron dynamics in human focal epilepsy. *Nat. Neurosci.* **14**, 635–641 (2011).

28. Mukamel, R. & Fried, I. Human intracranial recordings and cognitive neuroscience. *Annu. Rev. Psychol.* **63**, 511–537 (2012).

29. Misra, A. *et al.* Methods for implantation of micro-wire bundles and optimization of single/multiunit recordings from human mesial temporal lobe. *J. Neural Eng.* **11**, 026013 (2014).

30. Cash, S. S. & Hochberg, L. R. The emergence of single neurons in clinical neurology. *Neuron* **86**, 79–91 (2015).

31. Merricks, E. M. *et al.* Single unit action potentials in humans and the effect of seizure activity. *Brain* **138**, 2891–2906 (2015).

32. Jamali, M. *et al.* Dorsolateral prefrontal neurons mediate subjective decisions and their variation in humans. *Nat. Neurosci.* **22**, 1010–1020 (2019).

33. Chari, A., Thornton, R. C., Tisdall, M. M. & Scott, R. C. Microelectrode recordings in human epilepsy: a case for clinical translation. *Brain Commun.* **2**, (2020).

bioRxiv preprint doi: https://doi.org/10.1101/2021.06.20.449152; this version posted June 21, 2021. The copyright holder for this preprint (which was not certified by peer review) is the author/funder, who has granted bioRxiv a license to display the preprint in perpetuity. It is made available under aCC-BY-ND 4.0 International license.

34. Vázquez-Guardado, A., Yang, Y., Bandodkar, A. J. & Rogers, J. A. Recent advances in neurotechnologies with broad potential for neuroscience research. *Nat. Neurosci.* (2020) doi:10.1038/s41593-020-00739-8.

35. Hochberg, L. R. *et al.* Neuronal ensemble control of prosthetic devices by a human with tetraplegia. *Nature* **442**, 164–171 (2006).

36. Hochberg, L. R. *et al.* Reach and grasp by people with tetraplegia using a neurally controlled robotic arm. *Nature* **485**, 372–375 (2012).

37. Simeral, J. D., Kim, S. P., Black, M. J., Donoghue, J. P. & Hochberg, L. R. Neural control of cursor trajectory and click by a human with tetraplegia 1000 days after implant of an intracortical microelectrode array. *J. Neural Eng.* **8**, (2011).

38. Collinger, J. L. *et al.* High-performance neuroprosthetic control by an individual with tetraplegia. *The Lancet* **381**, 557–564 (2013).

39. Aflalo, T. *et al.* Decoding motor imagery from the posterior parietal cortex of a tetraplegic human. *Science* **348**, 906–910 (2015).

40. Flesher, S. N. *et al.* Intracortical microstimulation of human somatosensory cortex. *Sci. Transl. Med.* **8**, 361ra141 (2016).

41. Ajiboye, A. B. *et al.* Restoration of reaching and grasping movements through brain-controlled muscle stimulation in a person with tetraplegia: a proof-of-concept demonstration. *The Lancet* **389**, 1821–1830 (2017).

42. Stavisky, S. D. *et al.* Neural ensemble dynamics in dorsal motor cortex during speech in people with paralysis. *eLife* **8**, 1–31 (2019).

43. Stavisky, S. D. *et al.* Speech-related dorsal motor cortex activity does not interfere with iBCI cursor control. *J. Neural Eng.* **17**, 016049 (2020).

44. Willett, F. R., Avansino, D. T., Hochberg, L. R., Henderson, J. M. & Shenoy, K. V. High-performance brain-to-text communication via handwriting. *Nature* **593**, 249–254 (2021).

bioRxiv preprint doi: https://doi.org/10.1101/2021.06.20.449152; this version posted June 21, 2021. The copyright holder for this preprint (which was not certified by peer review) is the author/funder, who has granted bioRxiv a license to display the preprint in perpetuity. It is made available under aCC-BY-ND 4.0 International license.

45. Venkataramani, V. *et al.* Glutamatergic synaptic input to glioma cells drives brain tumour progression. *Nature* **573**, 532–538 (2019).

46. Venkatesh, S. *et al.* Electrical and synaptic integration of glioma into neural circuits. *Nature* **573**, 539–545 (2019).

47. Mitchell, J. F., Sundberg, K. A. & Reynolds, J. H. Differential Attention-Dependent Response Modulation across Cell Classes in Macaque Visual Area V4. *Neuron* **55**, 131–141 (2007).

48. Pachitariu, M., Steinmetz, N., Kadir, S., Carandini, M. & Harris, K. Fast and accurate spike sorting of high-channel count probes with KiloSort. *Adv. Neural Inf. Process. Syst.* **2016**, 1–9 (2016).

49. Zhu, S., Xia, R., Chen, X. & Moore, T. Heterogeneity of Neuronal Populations within Columns of Primate V1 Revealed by High-Density Recordings. *bioRxiv* (2020) doi:10.1101/2020.12.22.424048.

50. Dickey, C. W. *et al.* Travelling spindles create necessary conditions for spike-timing-dependent plasticity in humans. *Nat. Commun.* **12**, 1027 (2021).

51. Lee, E. K. *et al.* Non-linear Dimensionality Reduction on Extracellular Waveforms Reveals Physiological, Functional, and Laminar Diversity in Premotor Cortex. *bioRxiv* 2021.02.07.430135 (2021).

52. McCormick, D. A., Connors, B. W., Lighthall, J. W. & Prince, D. A. Comparative electrophysiology of pyramidal and sparsely spiny stellate neurons of the neocortex. *J. Neurophysiol.* **54**, 782–806 (1985).

53. Bartho, P. *et al.* Characterization of Neocortical Principal Cells and Interneurons by Network Interactions and Extracellular Features. *J. Neurophysiol.* **92**, 600–608 (2004).

54. Snyder, A. C., Morais, M. J. & Smith, M. A. Dynamics of excitatory and inhibitory networks are differentially altered by selective attention. *J. Neurophysiol.* **116**, 1807–1820 (2016).

55. Sun, S. H. *et al.* Analysis of extracellular spike waveforms and associated receptive fields of neurons in cat primary visual cortex. *J. Physiol.* **8**, 2211–2238 (2021).

bioRxiv preprint doi: https://doi.org/10.1101/2021.06.20.449152; this version posted June 21, 2021. The copyright holder for this preprint (which was not certified by peer review) is the author/funder, who has granted bioRxiv a license to display the preprint in perpetuity. It is made available under aCC-BY-ND 4.0 International license.

56. Kaufman, M. T. *et al.* Roles of monkey premotor neuron classes in movement preparation and execution. *J. Neurophysiol.* **104**, 799–810 (2010).

57. Kaufman, M. T., Churchland, M. M. & Shenoy, K. V. The roles of monkey M1 neuron classes in movement preparation and execution. *J. Neurophysiol.* **110**, 817–825 (2013).

58. Swadlow, H. A. Fast-spike interneurons and feedforward inhibition in awake sensory neocortex. *Cereb. Cortex* **13**, 25–32 (2003).

59. Swadlow, H. A. Efferent neurons and suspected interneurons in motor cortex of the awake rabbit: axonal properties, sensory receptive fields, and subthreshold synaptic inputs. *J. Neurophysiol.* **71**, 437–453 (2017).

60. Janca, R. *et al.* Detection of Interictal Epileptiform Discharges Using Signal Envelope Distribution Modelling: Application to Epileptic and Non-Epileptic Intracranial Recordings. *Brain Topogr.* **28**, 172–183 (2015).

61. Lewis, L. D. *et al.* Local cortical dynamics of burst suppression in the anaesthetized brain. *Brain* **136**, 2727–2737 (2013).

62. Westover, M. B. *et al.* Real-time segmentation of burst suppression patterns in critical care EEG monitoring. *J. Neurosci. Methods* **219**, 131–141 (2013).

63. Hodge, R. D. *et al.* Conserved cell types with divergent features between human and mouse cortex. *Nature* 384826 (2018) doi:10.1101/384826.

64. Boldog, E. *et al.* Transcriptomic and morphophysiological evidence for a specialized human cortical GABAergic cell type. *Nat. Neurosci.* **21**, 1185–1195 (2018).

65. Hodge, R. D. *et al.* Transcriptomic evidence that von Economo neurons are regionally specialized extratelencephalic-projecting excitatory neurons. *Nat. Commun.* **11**, (2020).

66. Ching, S., Purdon, P. L., Vijayan, S., Kopell, N. J. & Brown, E. N. A neurophysiological – metabolic model for burst suppression. *Proc. Natl. Acad. Sci. USA* **109**, 3095–3100 (2012).

67. Peyrache, A. *et al.* Spatiotemporal dynamics of neocortical excitation and inhibition during human sleep. *Proc. Natl. Acad. Sci.* **109**, 1731–1736 (2012).

bioRxiv preprint doi: https://doi.org/10.1101/2021.06.20.449152; this version posted June 21, 2021. The copyright holder for this preprint (which was not certified by peer review) is the author/funder, who has granted bioRxiv a license to display the preprint in perpetuity. It is made available under aCC-BY-ND 4.0 International license.

68. Felsenstein, O. & Peled, N. *MMVT – Multi-Modality Visualization Tool*. *GitHub Repository* (2017). doi:10.5281/zenodo.438343.

69. Ulbert, I., Heit, G., Madsen, J., Karmos, G. & Halgren, E. Laminar analysis of human neocortical interictal spike generation and propagation: Current source density and multiunit analysis in vivo. *Epilepsia* **45**, 48–56 (2004).

70. Halgren, M. *et al.* The generation and propagation of the human alpha rhythm. *Proc. Natl. Acad. Sci. U. S. A.* **116**, 23772–23782 (2019).

71. Buccino, A. P. *et al.* Combining biophysical modeling and deep learning for multielectrode array neuron localization and classification. *J. Neurophysiol.* **120**, 1212–1232 (2018).

72. Musk, E. & Neuralink. An integrated brain-machine interface platform with thousands of channels. *bioRxiv* 703801 (2019) doi:10.1101/703801.

73. Dutta, B. *et al.* The Neuropixels probe: A CMOS based integrated microsystems platform for neuroscience and brain-computer interfaces. *2019 IEEE Int. Electron Devices Meet. IEDM* 10.1.1-10.1.4 (2019) doi:10.1109/IEDM19573.2019.8993611.

bioRxiv preprint doi: https://doi.org/10.1101/2021.06.20.449152; this version posted June 21, 2021. The copyright holder for this preprint (which was not certified by peer review) is the author/funder, who has granted bioRxiv a license to display the preprint in perpetuity. It is made available under aCC-BY-ND 4.0 International license.

METHODS (COMPLETE ONLINE VERSION).

Patients & clinical/research electrode placement

All patients voluntarily participated after informed consent according to NIH guidelines as monitored by the Partners Institutional Review Board (IRB) Massachusetts General Hospital (MGH). Participants were informed that participation in the experiment would not alter their clinical treatment in any way, and that they could withdraw at any time without jeopardizing their clinical care. Recordings in the operating room were acquired with 9 participants (mean= 59 years old, ranging from 34 to 75; 7 female; **Supplemental Table 1**) who were already scheduled for a craniotomy for concurrent clinical intraoperative neurophysiological monitoring or testing for mapping motor, language, and sensory regions and removal of tissue as a result of tumor or epilepsy or undergo intra-operative neurophysiology as part of their planned deep brain stimulator (DBS) placement [1–4]. Prior to inserting the Neuropixels probe, a small superficial incision in the pia was done using an arachnoid surgical knife. The Neuropixels probe was inserted through this incision. Recordings were referenced to sterile ground and recording reference needle electrodes (Medtronic) placed in nearby muscle tissue (often scalp) as deemed safe by the neurosurgical team though a series of tests ground and reference tests were performed to identify the ideal combinations of ground and reference options, listed below (**Supplemental Table 1**).

Following the surgery, the preoperative T1-weighted MRI was used to generate a 3D surface brain map using FreeSurfer scripts [5–7] (http://surfer.nmr.mgh.harvard.edu). Images obtained during surgery and locations as indicated using Brainlab (Brainlab, Inc.) captured during the surgery were aligned to the 3D reconstructions using Blender software (https://www.blender.org/) and MMVT [7–9]. The method involved projecting the surgical image onto the patient's reconstructed brain using Blender and then placing a 3D model of the Neuropixels probe on that location similar to other coregistration approaches [4,7,8,10]. Angles were calculated from photographs taken during the surgery as well as trajectories limited by the location and angle of the burr hole for DBS surgery.

Neuropixels recordings, data collection & analysis

Neuropixels probes (NP v 1.0, version S, IMEC) sterilized with Ethylene Oxide (BioSeal) were connected to a 3B2 IMEC headstage wrapped in a sterile plastic bag and sealed using TegaDerm (3M) to keep the field sterile. Neuropixels probes (NP v 1.0-S, IMEC) include an electrode shank (width: 70µm, length: 10 mm, thickness: 100µm) of 960 total sites laid out in a checkerboard pattern with contacts at ~18 µm site to site distances (16 µm (column), 20 µm

bioRxiv preprint doi: https://doi.org/10.1101/2021.06.20.449152; this version posted June 21, 2021. The copyright holder for this preprint (which was not certified by peer review) is the author/funder, who has granted bioRxiv a license to display the preprint in perpetuity. It is made available under aCC-BY-ND 4.0 International license.

(row); [11]). Handling of the electrodes and the headstage from outside the sterile bag was all performed in sterile conditions in the operating room. The headstage was connected via a multiplexed cable to a PXIe acquisition module card (IMEC), installed into a PXIe Chassis (PXIe-1071 chassis, National Instruments). All Neuropixels recordings were performed using SpikeGLX (http://billkarsh.github.io/SpikeGLX/) on a computer connected to the PXIe acquisition module recording the action potential band (AP, band-pass filtered from 0.3-10 kHz) sampled at 30 kHz and a local field potential band (LFP, band-pass filtered from 0.5-500 Hz), sampled at 2.5 kHz [11–13]. Since these Neuropixels probes enable 384 recording channels which can then be used to address 960 electrodes across the probe shank, we tested different electrode maps which allowed us to record different portions of the probe. One map allowed for recording the lower portion of the probe (the most distal channels). A second map allowed for recording two rows along the entire length of the electrode. This map was used to identify the depth of the electrode in the cortex and we switched to the distal tip map (short map) for the main recording. A final map allowed for recording in a series of tetrode locations, skipping rows to distribute recordings along the entire length of the probe.

Synchronization was performed through two different approaches. TTL triggers via a parallel port produced either during a task via MATLAB or custom code from a separate computer were sent to both the National Instruments and IMEC recording systems, via a parallel port system. In addition, we used the TTL output to send the synchronization trigger via the SMA input to the IMEC PXIe acquisition module card to allow for added synchronizing triggers which were also recorded on an additional breakout analog and digital input/output board (BNC-2110, National Instruments) connected via a PXIe board (PXIe-6341 module, National Instruments). The TTL triggers were produced either during a task via MATLAB or custom code on the task computer.

Recording challenges and lessons learned

Five main challenges were faced when performing these recordings: 1) sterilization and maintaining a sterile field and conditions; 2) electrode fracture and disconnects; 3) decreasing noise in the recordings through referencing; 4) external sources of noise; 5) mechanical stabilization (**Fig. 1**; **Supplemental Fig. 1**).

Sterilization and maintaining a sterile field

To ensure we could use the Neuropixels probes in the OR, we worked with BioSeal (Placentia, CA) and sent them a sample of 25 Neuropixels probes. BioSeal took the samples through a validation process to determine that ethylene oxide (EtO) could be used to sterilize

bioRxiv preprint doi: https://doi.org/10.1101/2021.06.20.449152; this version posted June 21, 2021. The copyright holder for this preprint (which was not certified by peer review) is the author/funder, who has granted bioRxiv a license to display the preprint in perpetuity. It is made available under aCC-BY-ND 4.0 International license.

the Neuropixels probes. We also tested whether working Neuropixels probes were operational before and after sterilization. An important part of the process was identifying safe sterile packaging for sterilization and transport. We found we could place the probes sideways inside a slightly modified EtO-safe sterile container (SteriBest Trays, Sterilization Instrument Tray, Instrument Tray Sizes (inches):Base, Lid, Mat 6x2.5x.75], item#A-CP614, from Duraline Biosystem; **Fig. 1a**; **Supplemental Fig. 1g**; **Supplemental Table 1**). When received the boxes, we clipped protruding silicone nubs in an area of 3 cm x 3 cm on one side of the box as well as a few silicone nubs on the other end of the box. We found that we could package and safely ship and handle the Neuropixel probe cross-country by weaving the Neuropixels ribbon cable around the vertical silicone nubs in the sterilization containers with the Neuropixels probe and headstage perpendicular to the base of the box. We performed several tests to demonstrate the probe consistently survived this shipment approach, including before and after sterilization. Before shipping for sterilization, we soldered on a 10 cm long male touchproof cable (the white cable in Fig. 1a, b and d) to the reference side of the Neuropixels probe. In addition, we labelled the lid of the box to track individual probes. The validation of 25 probes performed by BioSeal was done with the Neuropixels probes in this configuration and with this specific SteriBest Tray packaging (including the added touchproof connection cable). Once shipped to Bioseal packed in bubble wrap, the company would return the probes in their sterilization boxes sealed in approved packaging. We have found this approach kept the electrodes intact and tracked throughout transport and sterilization.

Electrode fractures and disconnects

We had instances of electrode fracture (N=2), both of which were with the thinner Neuropixels 1.0 probes (thickness: 25µm, width: 70µm, length: 10 mm). We then switched to a thicker custom Neuropixels 1.0-S probe (thickness: 100µm width: 70 µm, length: 10 mm) for the remaining recordings and, of the 7 uses of thick probes, we only had one instance of electrode fracture. In each instance, we documented whether the probes were intact afterward both via the SpikeGLX software and through thorough photograph documentation. In the three probes which were fractured, we were able to photograph the pieces to reconstruct the entire probe do validate probe recovery. In the remaining probes, the photographs after the case confirmed the electrodes were fully intact after the case. In addition, in the intact probes after the case, software check via SpikeGLX involved a hardware check indicating the probes were intact and fully functioning.

Decreasing noise using referencing and grounding

bioRxiv preprint doi: https://doi.org/10.1101/2021.06.20.449152; this version posted June 21, 2021. The copyright holder for this preprint (which was not certified by peer review) is the author/funder, who has granted bioRxiv a license to display the preprint in perpetuity. It is made available under aCC-BY-ND 4.0 International license.

Even though we had tested the Neuropixels probe as well as had considerable experience in using Neuropixels in NHPs which informed how we built our electrophysiological system [13], we found moving the Neuropixels recordings into the human OR was made much more difficult with considerable added noise compared to any of the other testing settings. In the first four tests, we followed the original recommendations to tie the reference to the ground on the Neuropixels probe which degraded the signal considerably in the OR (**Supplemental Fig. 1a**). The signal was substantially improved by separating the ground and reference on the Neuropixels probe, with a single Medtronic sterile wire connected to the reference placed in the scalp and a separate wire attached to the ground and also placed in the scalp as deemed safe by the neurosurgical team. Improving the signal also involved tying the patient ground to the recording ground the patient to the recording via a BOVIE pad (Clearwater, FL) connected to the grounding BNC on the NIDAQ board used for the Neuropixels system. Placing the grounding lead into saline or CSF degraded the signal by saturating the LFP and increasing noise in the system.

External sources of noise

Changing the reference from the external reference in the software (using SpikeGLX) to the internal reference also increased noise significantly (**Supplemental Fig. 1c**). We also discovered an external source of noise was the wall-powered anesthesia IV pump (as is commonly used during patient transport) which, when unplugged and operating on battery, would decrease the physiological noise. Finally, we did a series of tests to determine if other signals added sources of noise and we did not find an effect of the BOVIE cautery machine, the ROSA robot, the lights or other machines in the room.

Mechanical stabilization

Two separate stabilization approaches were tested. One approach involved the patients receiving DBS implantations at MGH, who normally also undergo standardized micro-electrode recording to optimize anatomical targeting [1,14], Neuropixels probes were inserted in the same locations as the microelectrodes that traverse the dorsal lateral surface of the prefrontal cortex on the way to the target nucleus, offering a brief chance to study neuronal dynamics in the dlPFC and not perturbing the planned operative approach nor alter clinical care [1–3,14–16]. Three cannulae were placed in a manipulator (AlphaOmega Engineering, Nazareth, Israel) and the Neuropixels probe was attached to the cannulae using SteriStrips (3M™ Steri-Strip™ Reinforced Adhesive Skin Closures). The manipulator was attached to the ROSA ONE® Brain (Zimmer Biomet) arm. The Neuropixels probe was put over the burr hole by the ROSA robot arm. ROSA was then used to move the probe insert the probe using fine millimeter steps, with

bioRxiv preprint doi: https://doi.org/10.1101/2021.06.20.449152; this version posted June 21, 2021. The copyright holder for this preprint (which was not certified by peer review) is the author/funder, who has granted bioRxiv a license to display the preprint in perpetuity. It is made available under aCC-BY-ND 4.0 International license.

some adjustment possible using the AlphaOmega micromanipulator.The second approach involved securing the Neuropixels probe to a sterile syringe which was then held by a 3-axis micromanipulator built for Utah array placement (BlackRock, Salt Lake City, UT) which was attached to a Greenberg retractor. The Neuropixels probe was in place and lowered using the micromanipulator.

Compensation for tissue movement and electrode alignment through time

We found clear evidence of vertical tissue movement relative to the Neuropixels probe in the local field potential (LFP) recordings (**Supplemental Fig. 2**). To confirm that this was due to movement of the tissue as well as effects of heartbeat, we aligned the movement artifact to the heartbeat in time (this was possible thanks to audio tracking of the EKG in 2 participants' cases). We found the movement roughly matched this tracking. To confirm that the manual tracking could match the movement of the brain relative to the electrode, we performed tissue-level tracking of the video recordings of the case and found we could align the filmed movement of the brain pumping relative to the electrode, which was well visualized in the LFP band across channels as tracked through time (**Supplemental Fig. 2b**). We tested several approaches to address this movement and correct for the alignment, including the Kilosort 3.0 drift adjustments and estimation (https://github.com/MouseLand/Kilosort) and spike time-informed alignment approaches (https://github.com/evarol/NeuropixelsRegistration). We chose to use the LFP-informed manual tracking as it was better-resolved in the time domain since the dynamic range of LFP allowed for per time step (0.0004 sec) alignment and interpolation. In contrast, the automatic approach depended on firing rate and arrival of spikes, which were sparse (**Fig. 1e-f**).

Manual tracking of movement using LFP signals

The signal was first extracted from the binary files into local field potential (LFP, <500 Hz filtered data, sampled at 2500 Hz) and action potential (AP, >500 Hz filtered data, sampled at 30000 Hz) from SpikeGLX using MATLAB and available preprocessing code (https://billkarsh.github.io/SpikeGLX/). We inspected the data visually as well as examined the timeline of the recording to reject noisy time ranges (such as during insertion.) We then further examined the voltage deflections in the LFP for a prominent, bounded deflection in the voltage where we observed the voltage values shifting in unison(**Supplemental Figure 2**) which was consistently present throughout the recording (blue or red bands in **Supplemental Figure 2**). We attempted to use a number of algorithms to detect these shifts, but the multiple changes present (heartrate, slow and mid-range drifting, and other shifts) were not effectively tracked by these algorithms. Instead, to capture the displacement in the movement bands, we imported the

bioRxiv preprint doi: https://doi.org/10.1101/2021.06.20.449152; this version posted June 21, 2021. The copyright holder for this preprint (which was not certified by peer review) is the author/funder, who has granted bioRxiv a license to display the preprint in perpetuity. It is made available under aCC-BY-ND 4.0 International license.

LFP voltage as an .stl file from MATLAB into Blender (https://www.blender.org/), a three dimensional animation program which allowed for easier manual tracing compared to MATLAB. Using the surface voltage and the Grease Pencil feature, we traced the shifting band of negatively deflecting LFP throughout the recording at a resolution of 500 Hz. The line produced then was exported as a .csv file and imported into MATLAB, where it was compared with the LFP at higher resolution to check whether the manual tracing matched the LFP displacement (**Supplemental Figure 2a**). This traced line information was upsampled to 2500 Hz to match the sampling frequency of the LFP channels (interp1, 'makima').

Preprocessing AP recordings

Once we had the LFP baseline to track probe movement through time, we then applied analyses to the AP sampled band. To account for differences in the channels before aligning the data (as channels can have differences in impedance), we first detrended data (which removes best fitted line to each channel), calculated the median, and subtracted it from all channels. We then normalized the voltage signal across channels by multiplying each channel's voltage time series by a normalization factor where *Normalized data = Channel signal * (1/std) * 600*. In this case, the *std* was the standard deviation of channel data without outliers, particularly epochs which were relatively quiet. We defined outliers as elements which were more than 1.5 interquartile ranges above the upper quartile or below the lower quartile of the distribution of voltage signals. Finally, we chose the value of 600 in the normalization to allow us to scale the data up to an int16 format for improved data resolution.

Alignment and interpolation of AP channels for manual registration

To then re-align the AP channel data so as to offset the movement artifact, we upsampled the traced line to 30KHz to match the AP sampling rate (interp1, 'makima'). We then, for each time bin, applied a spatial interpolation between channels vertically in two columns of the Neuropixels recording, resulting in a vertical spatial resolution of 1um. (**Supplemental Figure 2**). These steps resulted in a large, high resolution interpolated matrix that we could then follow through time. This let us compensate for the movement effects by resampling the voltage in space (**Supplemental Figure 2**) based on the manually registered movement trajectory described in "Manual Tracking of Movement using LFP signals".

Specifically, for each time bin, we shifted the vertical channels vector up or down according the upsampled traced line, resulting in >450 'virtual channels' that each contained voltage information putatively from a specific brain location. Finally, since the virtual channels on

bioRxiv preprint doi: https://doi.org/10.1101/2021.06.20.449152; this version posted June 21, 2021. The copyright holder for this preprint (which was not certified by peer review) is the author/funder, who has granted bioRxiv a license to display the preprint in perpetuity. It is made available under aCC-BY-ND 4.0 International license.

both ends (top and bottom of the shank) contained only partial data (due to brain movement relative to the electrode), we selected a subset of 384 virtual channels that contained the most continuous information throughout the recording (and did not shift channels into the edge), which could be inferred from the average channel offset.

Unit isolation and clustering

Single unit sorting was performed using Kilosort 3.0 [17] (https://github.com/MouseLand/Kilosort) as well as Phy (https://github.com/cortex-lab/phy) and then manually curated using in-house MATLAB code to visually inspect the template as well as the waveforms assigned to each cluster. The Kilosort 3.0 parameters included: Nblocks = 0 – as no additional registration was needed according to spiking activity after the manual registration; Threshold [10, 11] to be more strict in our detections (initial values were [9,9] which resulted in ~800 units for Pt. 02). Clusters were merged in Phy if the templates were similar between clusters, the spatial spread of waveforms were highly similar and overlapping, and cross-correlations of the event times indicated high levels of correlation. To further process and shift each individual waveform to correct for Kilosort3 misalignment, we also calculated the cross correlation of individual waveforms with the cluster template and adjusted waveforms according to location of maximal voltage value per waveform in the sampled time.

Waveform feature analyses and classification

Clusters were then separated into single units and multi-unit activity (MUA). Units were classified as MUA if there was a mixture of distinct waveforms (examined in Phy) as well as a complicated (and abnormal) autocorrelogram. For all units, we then measured the spike duration, halfwidth, peak-trough ratio, repolarization slope, recovery slope, and amplitude measures (**Fig. 2**; adapted from [12]; https://github.com/jiaxx/waveform_classification). Further, we applied the spatial spread and velocity measures to each cluster to identify whether we could observe evidence for backpropagating action potentials or other unique spatial dynamics (**Fig. 2**; adapted from [12]).

We used three different classification approaches to group the units. First, using a standard approach, units were grouped into regular spiking (RS), fast spiking (FS), positive spikes (PS) classifications based on the spike waveform duration (valley-to-peak) of the largest peak across channels per unit [18–23]. The ranges for each classification were as follows: negative going peaks included FS (duration <0.3 ms) and RS (duration>0.3 ms) and positive spikes (PS). Second, we applied principal components analyses on the first six channels per unit and

bioRxiv preprint doi: https://doi.org/10.1101/2021.06.20.449152; this version posted June 21, 2021. The copyright holder for this preprint (which was not certified by peer review) is the author/funder, who has granted bioRxiv a license to display the preprint in perpetuity. It is made available under aCC-BY-ND 4.0 International license.

clustered these average waveforms using k-means clustering (squared Euclidean distance, 1000 replicates, 1000 maximum iterations) into 7 clusters based on the separability of the clusters (using silhouette) and how clean the resulting clusters were. Finally, we used a novel non-linear method, WaveMAP, which took into account the spatial and temporal waveform characteristics while separating out differences in the waveforms [24]. WaveMAP includes a combination of dimensionality reduction with Universal Manifold Approximation and Projection (UMAP) combined with Louvain clustering to identify clusters in the data set [24]. We then compared the waveform features across these different classifications.

Local field potential analyses

Custom MATLAB code (version R2020a) in combination with open source code from the Fieldtrip toolbox ([25]; http://www.fieldtriptoolbox.org/).

Burst suppression ratio measurement

The burst suppression ratio (BSR) was computed using an automated method [26,27] (https://github.com/drasros/bs_detector_icueeg). After averaging the LFP across all channels, this method then labels each time sample as either burst or suppression. Briefly, the method uses the previous data with each channel and applies the following equations:

$$\mu t = \beta\ \mu t\text{-}1 + (1\text{-}\beta)\ xt$$

$$\sigma t2 = \beta\ \sigma t\text{-}12 + (1\text{-}\beta)\ (xt - \mu t)2$$

$$zt = \delta[\sigma t2 < \theta]$$

Where xt is the value of the normalized signal of one channel at time t, μt and σt2 are current values of the recursively estimated local mean and variance, respectively. Finally, zt is an indicator function that labels each data point as either a burst (0) or suppression (1). The value of β determines the balance between the effect of recent and past data set based on previously trained data [26]. The classification threshold θ (i.e., the value above which a data point should be classified as burst) was adjusted to evaluate our dataset visually with values of θ = 50, 100, 150, and 200 and was informed by the input from two experts who reviewed selected intervals to identify burst and suppression using each possible theta value. The value of θ = 200 was selected to reliably identify burst and suppression induced by general anesthesia. The burst suppression ratio for each recording in an anesthetized patient (N=2) was evaluated as the proportion of suppression-labeled samples in a moving window (1 s duration, no overlap).

Inter-ictal epileptiform discharges

bioRxiv preprint doi: https://doi.org/10.1101/2021.06.20.449152; this version posted June 21, 2021. The copyright holder for this preprint (which was not certified by peer review) is the author/funder, who has granted bioRxiv a license to display the preprint in perpetuity. It is made available under aCC-BY-ND 4.0 International license.

In one case, the Neuropixels electrode was inserted into the lateral temporal lobe before tissue resection for epilepsy. As we could identify interictal epileptiform discharges (IIDs) in the LFP, we applied both an automatic and a visual detection approach to verify the timing and location of the IIDs in the Neuropixels recording. For automatic detection, we averaged the LFP across channels and applied the algorithm of [28], version v21, default settings except -h at 60 and -k1 at 7 to increase the threshold for detection; http://isarg.fel.cvut.cz), which adaptively models distributions of signal envelopes to discriminate IIDs from LFP [28]. In addition, a trained and experienced epileptologist (SSC) examined the average LFPs and confirmed the timing of the detected IIDs. This two-step process was necessary as the burst suppression from the anesthesia produced waveforms which could obscure the IIDs. For several analyses, the single unit spike times were then aligned relative to the peaks of the IIDs.

Statistical analysis

All statistical comparisons were performed using non-parametric measures, so we did not test for normality. Multiple comparisons tests were performed using the Kruskal–Wallis test for non-equivalence of multiple medians followed post hoc Tukey-Kramer method to identify statistically separable groups. For comparisons between individual medians, we used the Wilcoxon rank-sum test (two-sided). We corrected by adjusting the target p-value (0.05) with a Bonferroni correction for the number of comparisons being done.

Data availability

The majority of the data that support the findings of this study are available from the corresponding author upon reasonable request, though a subset of data will be available for download at Dryad (https://datadryad.org/stash) upon publication.

Code availability

Open source acquisition software, SpikeGLX (http://billkarsh.github.io/SpikeGLX/) and record the neural data. Single unit sorting was performed using Kilosort 3.0 [17] (https://github.com/MouseLand/Kilosort) as well as Phy (https://github.com/cortex-lab/phy) Custom Matlab code (version R2020a) and python code in combination with open source code from the Fieldtrip toolbox (http://www.fieldtriptoolbox.org/) was used for the majority of the analyses with some code involving manual alignment available on Github (https://github.com/Center-For-Neurotechnology/CorticalNeuropixelProcessingPipeline). The burst suppression ratio (BSR) was computed using an automated method [26,27]

bioRxiv preprint doi: https://doi.org/10.1101/2021.06.20.449152; this version posted June 21, 2021. The copyright holder for this preprint (which was not certified by peer review) is the author/funder, who has granted bioRxiv a license to display the preprint in perpetuity. It is made available under aCC-BY-ND 4.0 International license.

(https://github.com/drasros/bs_detector_icueeg). Reconstruction of electrode locations and the manual tracing was done using the open source, free software Blender (https://www.blender.org/).

METHODS REFERENCES

1. Patel, S. R. *et al.* Studying task-related activity of individual neurons in the human brain. *Nat. Protoc.* **8**, 949–957 (2013).
2. Jamali, M. *et al.* Dorsolateral prefrontal neurons mediate subjective decisions and their variation in humans. *Nat. Neurosci.* **22**, 1010–1020 (2019).
3. Jamali, M. *et al.* Single-neuronal predictions of others' beliefs in humans. *Nature* **591**, 610–614 (2021).
4. Paulk, A. C. *et al.* Microscale Physiological Events on the Human Cortical Surface. *Cereb. Cortex* (2021) doi:10.1093/cercor/bhab040.
5. Reuter, M., Rosas, H. D. & Fischl, B. Highly Accurate Inverse Consistent Registration: A Robust Approach. *NeuroImage* **53**, 1181–1196 (2010).
6. Reuter, M., Schmansky, N. J., Rosas, H. D. & Fischl, B. Within-Subject Template Estimation for Unbiased Longitudinal Image Analysis. *NeuroImage* **61**, 1402–1418 (2012).
7. Dykstra, A. R. *et al.* Individualized localization and cortical surface-based registration of intracranial electrodes. *Neuroimage* **59**, 3563–3570 (2012).
8. Holmes, C. J. *et al.* Enhancement of MR Images Using Registration for Signal Averaging. *J. Comput. Assist. Tomogr.* **22**, 324–333 (1998).
9. Felsenstein, O. & Peled, N. *MMVT – Multi-Modality Visualization Tool*. *GitHub Repository* (2017). doi:10.5281/zenodo.438343.
10. Postelnicu, G., Zöllei, L. & Fischl, B. Combined Volumetric and Surface Registration. *IEEE Trans. Med. Imaging* **28**, 508–522 (2009).
11. Jun, J. J. *et al.* Fully integrated silicon probes for high-density recording of neural activity. *Nature* **551**, 232–236 (2017).

bioRxiv preprint doi: https://doi.org/10.1101/2021.06.20.449152; this version posted June 21, 2021. The copyright holder for this preprint (which was not certified by peer review) is the author/funder, who has granted bioRxiv a license to display the preprint in perpetuity. It is made available under aCC-BY-ND 4.0 International license.

12. Jia, X. *et al.* High-density extracellular probes reveal dendritic backpropagation and facilitate neuron classification. *J. Neurophysiol.* **121**, 1831–1847 (2019).
13. Trautmann, E. M. *et al.* Accurate Estimation of Neural Population Dynamics without Spike Sorting. *Neuron* **103**, 292-308.e4 (2019).
14. Amirnovin, R., Williams, Z. M., Cosgrove, G. R. & Eskandar, E. N. Experience with microelectrode guided subthalamic nucleus deep brain stimulation. *Neurosurgery* **58**, ONS96-102 (2006).
15. Sheth, S. a *et al.* Human dorsal anterior cingulate cortex neurons mediate ongoing behavioural adaptation. *Nature* **488**, 218–21 (2012).
16. Mian, M. K. *et al.* Encoding of rules by neurons in the human dorsolateral prefrontal cortex. *Cereb. Cortex* **24**, 807–816 (2014).
17. Pachitariu, M., Steinmetz, N., Kadir, S., Carandini, M. & Harris, K. Fast and accurate spike sorting of high-channel count probes with KiloSort. *Adv. Neural Inf. Process. Syst.* **2016**, 1–9 (2016).
18. McCormick, D. A., Connors, B. W., Lighthall, J. W. & Prince, D. A. Comparative electrophysiology of pyramidal and sparsely spiny stellate neurons of the neocortex. *J. Neurophysiol.* **54**, 782–806 (1985).
19. Bartho, P. *et al.* Characterization of Neocortical Principal Cells and Interneurons by Network Interactions and Extracellular Features. *J. Neurophysiol.* **92**, 600–608 (2004).
20. Mitchell, J. F., Sundberg, K. A. & Reynolds, J. H. Differential Attention-Dependent Response Modulation across Cell Classes in Macaque Visual Area V4. *Neuron* **55**, 131–141 (2007).
21. Snyder, A. C., Morais, M. J. & Smith, M. A. Dynamics of excitatory and inhibitory networks are differentially altered by selective attention. *J. Neurophysiol.* **116**, 1807–1820 (2016).
22. Dickey, C. W. *et al.* Travelling spindles create necessary conditions for spike-timing-dependent plasticity in humans. *Nat. Commun.* **12**, 1027 (2021).

bioRxiv preprint doi: https://doi.org/10.1101/2021.06.20.449152; this version posted June 21, 2021. The copyright holder for this preprint (which was not certified by peer review) is the author/funder, who has granted bioRxiv a license to display the preprint in perpetuity. It is made available under aCC-BY-ND 4.0 International license.

23. Sun, S. H. *et al.* Analysis of extracellular spike waveforms and associated receptive fields of neurons in cat primary visual cortex. *J. Physiol.* **8**, 2211–2238 (2021).

24. Lee, E. K. *et al.* Non-linear Dimensionality Reduction on Extracellular Waveforms Reveals Physiological, Functional, and Laminar Diversity in Premotor Cortex. *bioRxiv* 2021.02.07.430135 (2021).

25. Oostenveld, R., Fries, P., Maris, E. & Schoffelen, J.-M. FieldTrip: Open source software for advanced analysis of MEG, EEG, and invasive electrophysiological data. *Comput. Intell. Neurosci.* **2011**, 156869 (2011).

26. Westover, M. B. *et al.* Real-time segmentation of burst suppression patterns in critical care EEG monitoring. *J. Neurosci. Methods* **219**, 131–141 (2013).

27. Salami, P., Borzello, M., Kramer, M. A., Westover, M. B. & Cash, S. S. Quantification of seizure termination patterns reveals limited pathways to seizure end. *medRxiv* (2021) doi:10.1101/2021.03.03.21252789.

28. Janca, R. *et al.* Detection of Interictal Epileptiform Discharges Using Signal Envelope Distribution Modelling: Application to Epileptic and Non-Epileptic Intracranial Recordings. *Brain Topogr.* **28**, 172–183 (2015).